Available online at www.sciencedirect.com

ScienceDirect

Geochimica et Cosmochimica Acta 253 (2019) 249–266

Geochimica et Cosmochimica Acta

www.elsevier.com/locate/gca

Germanium isotopes and Ge/Si fractionation under extreme tropical weathering of basalts from the Hainan Island, South China

Hua-Wen Qi [a,*], Rui-Zhong Hu [a], Ke Jiang [a,b], Ting Zhou [a], Yue-Fu Liu [a,b], Yan-Wen Xiong [a,b]

[a] State Key Laboratory of Ore Deposit Geochemistry, Institute of Geochemistry, Chinese Academy of Sciences, Guiyang 550081, China
[b] University of Chinese Academy of Sciences, Beijing 100049, China

Received 10 July 2018; accepted in revised form 19 March 2019; available online 26 March 2019

Abstract

Chemical weathering of silicate rocks controls the fluvial input of dissolved Ge and Si into the ocean, and has substantial influence on the global Ge and Si geochemical cycles. The heavier dissolved Ge isotope compositions in the rivers (relative to the bulk silicate earth) suggest preferential incorporation of light isotopes into secondary weathering products during rock weathering (Baronas et al., 2017a). In this paper, we present the Ge isotope and Ge/Si ratio variations in the solid weathering products (soil and saprolite) from a well-developed basalt weathering profile (>15 m thick, including soil, saprolite, semi-weathered rock and fresh basalt) on the tropical island of Hainan (South China). We discussed the elemental/isotopic fractionation mechanism and the possible influence of major oxide composition on Ge isotope fractionation during extreme weathering of basalts in tropical climate. The Ge content ([Ge] = 2.19–4.12 ppm, 2.93 ppm on average, n = 52) and Ge/Si ratios (5.55–13.7 μmol/mol, 7.42 μmol/mol on average, n = 52) of solid weathering products are distinctly higher than those of the fresh basalts (avg. [Ge] = 1.64 ppm, Ge/Si = 2.66 μmol/mol, n = 5). The δ^{74}Ge values of solid weathering products range from -0.02 ± 0.10‰ (2σ) to 0.63 ± 0.10‰ (2σ), and exhibits complex stratigraphic variation across the weathering profile. There are no distinct correlations between the concentrations of Ge (or the Ge/Si ratio and δ^{74}Ge values) and SiO_2, Al_2O_3, Fe_2O_3 and MnO for most of the soil and saprolite samples. The distinct positive δ^{74}Ge vs. Ge (or τ_{Ge} value and Ge/Si ratio) correlations for most soil and saprolite samples indicate that the enrichment (or depletion) of Ge content, Ge isotopes and Ge/Si fractionation are controlled by a common sorption process of solid weathering products. The predicted opposite relationships between Ge/Si ratios and δ^{74}Ge values for pore water and that for solid weathering products can be evidenced by the positive Ge/Si vs. δ^{74}Ge correlation in the Wenchang basalt weathering profile and a negative one in the river water (Baronas et al., 2017a). Moreover, the estimated negative $\Delta^{74}Ge_{solid\text{-}dissolved}$ (1000 * Ln(α)) value (-1.38 ± 0.28‰ (2σ)) indicates that solid weathering products are a sink for light Ge isotopes, possibly balancing the isotopic budget with heavy Ge isotope compositions in global rivers and oceans.

Keywords: Ge isotopes; Ge/Si ratio; Chemical weathering; Basalt; Hainan Island (South China)

* Corresponding author.
E-mail address: qihuawen@vip.gyig.ac.cn (H.-W. Qi).

https://doi.org/10.1016/j.gca.2019.03.022
0016-7037/

1. INTRODUCTION

Chemical weathering of silicate minerals has important roles in soil development, nutrient availability in terrestrial and marine ecosystems, buffering of acid rain, and long-term atmospheric CO_2 regulation (Walker et al. 1981; Berner et al., 1983; Gaillardet et al., 1999; Brandy and Carroll, 1994). Two sources, (1) continental weathering and (2) high-temperature metasomatism of midocean ridge (MOR) mafic rocks, were suggested to dominate the delivery of germanium (Ge) to the oceans (Froelich et al., 1985, 1992; Mortlock and Froelich, 1986; Mortlock et al., 1993; King et al., 2000; McManus et al., 2003; Wheat and McManus, 2005). In recent years, significant progress has been made in using Ge isotopes and Ge/Si ratios to trace marine geochemical cycles of Ge and Si (Rouxel et al, 2006; Escoube et al., 2015; Baronas et al., 2016, 2017a; Guillermic et al., 2017; Rouxel and Luais, 2017). Such research demonstrated significant geochemical differences between the source-sink fluxes of Ge and Si in the marine system. However, few studies are dedicated to the Ge isotope fractionation during chemical weathering of silicate rocks.

Germanium is a trace element in the Earth's crust and natural waters (Bernstein, 1985; Taylor and McLennan, 1985; Arnórsson (1984)). Germanium and Si exhibit substantial geochemical differences during silicate rock weathering. For example, intensely-weathered soils developed on basaltic soil chronosequence in the Hawaiian Islands have higher bulk soil Ge/Si ratios (10–25 μmol/mol) than those of fresh basalt (2.5 μmol/mol). In addition, soil Ge concentrations increase with Si, and decrease with Fe, suggesting that Ge sequestration is related to the accumulation of secondary soil silicates, rather than the retention of Fe oxy-hydroxides in soil (Kurtz et al., 2002). The elevated soil Ge/Si ratios reflect partitioning of Ge into secondary clay minerals, plus additional retention of Ge by refractory non-silicates (Scribner et al., 2006). Soils and saprolites developed on granitic rocks show less pronounced Ge/Si fractionation (Ge/Si ratios: 2.6–3.6 μmol/mol; Kurtz et al., 2002; 1.1–3.0 μmol/mol; Lugolobi et al., 2010) than those developed on basaltic rocks. Ge/Si ratios in granitic soils and saprolites are strongly influenced by the relative weathering rates of the primary minerals (Kurtz et al., 2002; Derry et al., 2006; Lugolobi et al., 2010).

Germanium is preferentially incorporated into weathering products (such as clay minerals in soils), leading to lower fluvial Ge/Si ratios relative to those of the bedrocks ($Ge/Si_{rocks} = 1.2–2.6$ μmol/mol from felsic to mafic rocks) (Mortlock and Froelich, 1987; Froelich et al., 1992; Kurtz et al., 2002; Anders et al., 2003). Ge/Si ratios in uncontaminated streams (0.3–1.2 μmol/mol) exhibit seasonal variations (Mortlock and Froelich, 1987) and appear to correlate positively with 1/Si (Murnane and Stallard, 1990; Froelich et al., 1992). This suggests that the Ge/Si ratios in streams could be approximated by mixing of Si from two sources: one from the weathering of primary minerals and the other from weathering of secondary clay minerals (Murnane and Stallard, 1990; Froelich et al., 1992). Lugolobi et al. (2010) suggested that pore water Si concentration generally decreases upward through the saprolite, then rises again in the shallow soil; whereas the pore water Ge/Si ratios (0.70–4.1 μmol/mol) generally increase upward through the saprolite and soil developed on diorite from Puerto Rico, and the lowest Ge/Si ratios (0.27–0.47 μmol/mol) of spring water and baseflow stream waters were regarded to reflect deep initial weathering reactions resulting in the precipitation of Ge-enriched kaolinite at the saprolite-bedrock interface.

The dissolved $\delta^{74}Ge$ compositions of some rivers from California, Hawaii, and Peru (2.0–5.6‰; Baronas et al., 2017a) are significantly heavier than those of silicate rocks ($\delta^{74}Ge = 0.4–0.7$‰; Escoube et al., 2012), from which the dissolved Ge is primarily derived. The observed negative riverine Ge/Si vs. $\delta^{74}Ge$ correlation suggests that light Ge isotopes are preferentially incorporated into secondary weathering products during rock weathering processes (Baronas et al., 2017a). Organic matter and Fe-oxyhydroxides, which tend to preferentially enrich light Ge isotopes (Li et al., 2009; Li and Liu, 2010; Qi et al., 2011; Pokrovsky et al., 2014), are abundant in the weathering environment and thus have the potential to fractionate Ge isotopes. Both chemical weathering (primary minerals and then progressively secondary ones, such as Fe and Al oxides and aluminosilicates) and river transport processes (buffering of Ge by sorption onto fluvial clays and surficial Fe hydroxides; Bernstein and Waychunas, 1987; Mortlock and Froelich, 1987; Pokrovsky and Schott (2002)) may lead to the observed heavier riverine $\delta^{74}Ge$ signature. Unfortunately, no $\delta^{74}Ge$ data of secondary weathering products are currently available to test the above hypothesis (Baronas et al., 2017a).

At present, (1) there is no specific report on the analytical method of Ge isotopes for solid weathering products (i.e., soil and saprolite). Rouxel et al. (2006) proposed techniques for the precise determination of Ge isotopes in various geological matrices (including silicates). Whether these techniques are suitable for solid weathering products needs to be evaluated, because different matrices usually yield different matrix effects; (2) the fractionation degree and the fractionation mechanism of Ge isotopes during silicate weathering are still unknown; (3) what is the relationship between Ge/Si and $\delta^{74}Ge$ of the solid weathering products? and (4) the influence of solid weathering products on global Ge-Si geochemical cycles needs further constrain. More catchment and soil profile studies are needed to address these questions. We recently reported the mineralogical and geochemical (major and trace element) variations across a well-developed basalt weathering profile (i.e., the soil, saprolite, semi-weathered basalt and fresh basalt horizons) from South China (Jiang et al., 2018). In this contribution, we conducted systematic Ge isotope composition analyses of these samples, revealed the stratigraphic variations of $\delta^{74}Ge$ and Ge/Si ratios, and discussed how Ge-Si and Ge isotopes are fractionated and their possible influence on the global Ge-Si geochemical cycles. Our results highlight the importance of progressive weathering on Ge/Si and Ge isotope fractionations during extreme weathering of basalts in tropical climate.

2. GEOLOGICAL SETTING AND SAMPLING

The island of Hainan is the biggest tropical island in South China. The tropical climate on the island is controlled by the East Asian monsoon, with average annual temperature of 25 °C (summer maximum temperature: 30–32 °C; winter minimum temperature: 18–20 °C) and annual rainfall of 800–2500 mm (average: 1500 mm), of which above 80% (rainfall) occurs during May to October (Ma et al., 2007). Cenozoic basalts are widely distributed in northern Hainan (Liu et al., 2015, Fig. 1a). Major rock types include tholeiitic basalt, basaltic andesite, alkaline basalt and dolerite (Liu et al., 2015). These basalts are commonly covered by laterite derived from basalt weathering.

The sampling site is located in a quarry on a flat hill, and the weathering profile is developed on the Miocene-Pliocene tholeiitic basalt in southwestern Wenchang (19°34′47.0″N, 110°38′42.6″E, Fig. 1a and b). Our field observations indicate that the regolith thickness varies widely, with the depth of regolith-rock boundary fluctuating from several meters to about 15 m. It appears that the regolith is thicker in the saddle than in other parts (e.g., bump) of the basement. The weathering profile is covered by vegetation. The profile (up to 19.73 m thick) can be divided into three horizons down depth (soil, saprolite and basalt). Two discontinuities (soil-saprolite and rock-regolith interfaces) were identified in terms of color, clay mineralogy and major/trace element compositions at 2.4 m and 15.28 m depth of the weathering profile (Fig. 1c).

The soil samples (WC-1 to WC-12) were collected continually downwards and across the soil horizon, and 19 saprolite samples (WC-13 to WC-31) were conducted in a 15–20 cm spacing, while the other 21 saprolite samples (WC-32 to WC-52) were collected continually along depths. The size of each sample is about 20 cm (length) * 20 cm (width) * 15–20 cm (height). One semi-weathered basalt (WC-53) was collected near the rock-regolith interface, and then five fresh basalt samples (WC-54 to WC-58) were sampled in a 0.6–1.3 m spacing. Samples near the top of the soil horizon contain plant roots and stems. The detailed profile and sample descriptions (including horizon, soil color, soil structure, influence of biological activity and soil particle size analysis results) were reported by Jiang et al. (2018). The soil and saprolite samples collected were dried naturally, and milled to 200 mesh (<75 μm) with a tungsten-carbide mill after removing the plant roots and stems.

The top 2.4 m of the profile is consisted of reddish homogenous soil. The soil-saprolite interface is marked by the maximum enrichments of Al_2O_3, Fe_2O_3, TiO_2, LOI and Cr, slight enrichments of P, and the maximum depletion of SiO_2, relative to other elements. This interface is also

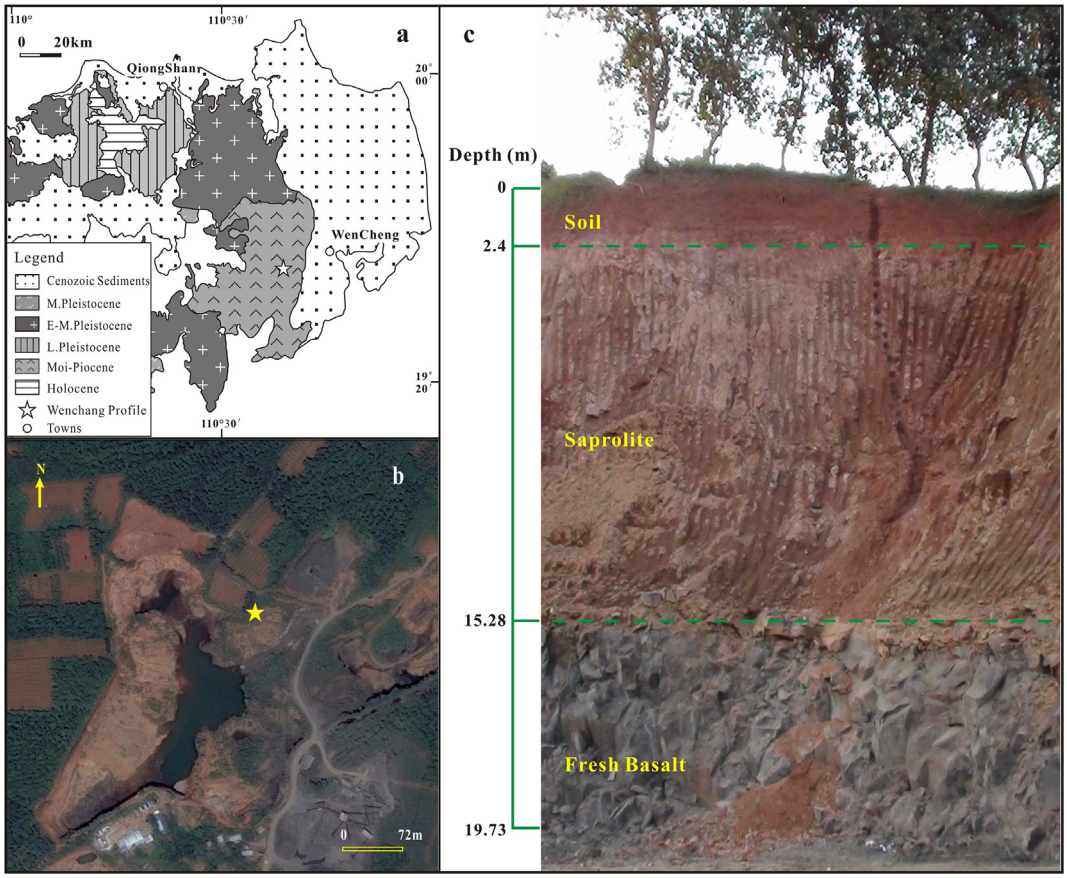

Fig. 1. (a) Simplified geologic map and sampling location in Wenchang, northern Hainan Island (modified after Liu et al., 2015); (b) Google Earth satellite image of the sampling site; (c) Outcrop photo of the Wenchang basalt weathering profile (after Jiang et al., 2018).

marked by the dominance of gibbsite and Fe-oxides/hydroxides and the color change from dark brick-red to light brick-red. The color of the saprolite changes from deep red at 2.4–13.2 m to yellowish at 13.2–15.28 m. The rock-regolith interface is marked by the presence of yellowish semi-weathered basalt that overlies parallelly on the fresh basalt, secondary phosphate, and distinct enrichments of Be, Cu, Zn, Ni, Sc and V (Jiang et al., 2018). The nearly constant Zr/Hf and Nb/Ta ratios of these soil, saprolite and basalt samples (Jiang et al., 2018), as well as saprolite Nd-Hf isotopes from basalt weathering profiles in the region (Ma et al., 2010), indicate that aeolian input is negligible, i.e., these weathering profiles were formed by in-situ extreme weathering of basaltic rocks.

3. METHODS

3.1. Sample dissolution and chemical purification

The sample dissolution and chemical purification processes basically followed the methods outlined by Rouxel et al. (2006). About 100 mg of soil and rock powders (200 mesh) were dissolved with 10 ml of concentrated HNO_3 in a closed PTFE beaker on a hot plate at 120 °C overnight. Subsequently, the vessels were opened and sample solutions were dried at the same condition. The residues were digested using 1 ml of concentrated HF and 5 ml of Milli-Q water in the sealed PTFE containers on a hot plate at 120 °C overnight. The solutions with possible precipitates were transferred into 50 ml plastic centrifuge tubes and were conditioned to ~1 N HF. After centrifuged, 20 ml (out of 35 ml) Ge-bearing supernatant was loaded onto an anion-exchange chromatographic column filled with 1.2 ml (wet volume) AG1-X8 resin (Bio-Rad, Hercules, USA; 100–200 mesh; chloride form; cat # 140–1441). The column was previously washed using 10 ml of 3 N HNO_3 and 10 ml of Milli-Q water, and was then conditioned with 1 N HF. After adsorption of Ge on the column, 10 ml of 1 N HF and 2 ml of Milli-Q water were successively passed through the column to elute the remaining matrices. Ge was then eluted with 12 ml of 3 N HNO_3, and the eluant was collected and taken to dryness on a hot plate at 80 °C. After evaporation, the solid residue was dissolved in 4.5 ml of 3 N HNO_3 and then 4 ml was loaded on a cation-exchange chromatographic column containing 2 ml AG50W-X8 resin (Bio-Rad, Hercules, CA, USA). The column was regenerated with 10 ml of 3 N HNO_3 and 10 ml of Milli-Q water, and conditioned with 0.28 N HNO_3. The solution that passed through the column contains Ge, whereas the residual matrix elements were strongly adsorbed on the resin. Complete recovery of Ge is assured after washing the column with 6 ml of 0.28 N HNO_3. After evaporation, the solid residue was re-dissolved in 3–5 ml of 0.28 N HNO_3 for more than two hours prior to Ge isotope analyses.

3.2. Measurement of Ge and Si concentrations

Germanium concentrations were measured using an ELAN DRC-e ICP-MS in the State Key Laboratory of Ore Deposit Geochemistry, Institute of Geochemistry, Chinese Academy of Sciences (IGCAS). About 50 mg of sample powder was weighted and placed into Teflon cups, and the sample was then decomposed by 1 ml HF and 0.5 ml concentrated HNO_3 at 185 °C for 24 h. After cooling and drying (and then re-drying after adding 1 ml concentrated HNO_3) over a hot plate, the residue was re-dissolved by 2 ml concentrated HNO_3 and 3 ml deionized water (500 ppb Rh were added as an internal standard for instrument drift corrections) at 140 °C for 5 h. After cooling, 0.4 ml of the sample solution was transferred into a 15 ml centrifugal tube and diluted to 8–10 ml for the ICP-MS measurement. A series of Merck standard solutions with different concentrations (0.1, 0.5, 1, 5, 10 and 100 ppb) were used to calibrate Ge concentrations or the intensities of ^{74}Ge in the final solution of soil and rock samples. Background Ge concentration in reagent blank (i.e., 0.28 N HNO_3 solution) was normally < 0.001 ppb. The analytical precision of Ge concentration analysis is estimated to be better than 5%, based on the comparison of measured and calibrated values for Merck standard solutions.

Major element (include Si) analyses of all soil and rock samples were conducted by using X Ray Fluorescence (XRF) at the ALS Laboratory in Guangzhou, China. Lithium-nitrate was added and mixed with the sample powder, and the mixed powder was then melted, poured into platinum crucibles and fused into glass beads, then the major element composition of all samples were analyzed using a PANalytical Magix Fast machine (with detection limit of >0.01%). Soil (GSS-4 and GSS-7) and rock (GSR-1) standard samples were used to monitor the analytical results, and the precision of major element (include Si) concentration is estimated to be better than 2% (Jiang et al., 2018).

3.3. Germanium isotope analyses

Germanium isotope analyses were performed on a Thermo Fisher Scientific Neptune Plus high resolution multi-collector (MC)-ICP-MS in the IGCAS. The detailed operating conditions and parameters are similar to those described in Rouxel et al. (2006) and Qi et al. (2011). The Neptune MC-ICP-MS instruments were operated at low mass resolution mode and on peak zero procedural blank correction. The intensities of ^{69}Ga, ^{70}Ge, ^{71}Ga, ^{72}Ge, ^{73}Ge and ^{74}Ge were monitored on L3, L2, L1, C, H1 and H2 Faraday cups, respectively. High-purity argon gas was used for sample introduction. Sample or standard solutions were introduced as hydrides through an on-line cold-vapor hydride generator system (HG, CETAC HGX-200) and introduced by a Minipuls 3 peristaltic pump (Gilson Corp., USA). Instrumental mass fractionations were corrected using the standard sample bracket (SSB) method with NIST SRM 3120a Ge standard solution (e.g. Qi et al., 2011; Escoube et al., 2012; Luais, 2012; Meng et al., 2015; Rouxel and Luais, 2017).

The 0.28 N HNO_3 blank solutions were used for washing before each sample or standard measurement, which yielded about 0.008 V, 0.009 V, 0.003 V and 0.012 V signals for ^{70}Ge, ^{72}Ge, ^{73}Ge and ^{74}Ge, respectively. The purified sample solutions were analyzed twice at a concentration

of 5–10 ppb. The 5 ppb NIST SRM 3120a Ge standard solutions generate 0.704 V, 0.978 V, 0.282 V and 1.354 V (on average, n = 30) signals for ^{70}Ge, ^{72}Ge, ^{73}Ge and ^{74}Ge, respectively, which are 85.5–110 times higher than the signals of corresponding isotopes in the 0.28 N HNO_3 blank solutions. The signals of 0.28 N HNO_3 blank solutions were monitored and deducted from the signals of true sample or standard solutions by an online system, before isotopic ratio calculation. The instrumental analyses comprised one block, which comprised 90 cycles with 1 s integration time per cycle. The average standard errors (abs) for $^{74}Ge/^{70}Ge$, $^{73}Ge/^{70}Ge$, $^{72}Ge/^{70}Ge$ and $^{74}Ge/^{72}Ge$ of NIST SRM3120a during a 90 s session are 0.000044, 0.000011, 0.000029, and 0.000022 (n = 500), respectively.

All values are reported relative to the Ge isotope reference standard NIST 3120a expressed in delta ($\delta^{74}Ge$) notation in ‰ units: $\delta^{74}Ge = [(^{74}Ge/^{70}Ge_{sample})/(^{74}Ge/^{70}Ge_{NIST\ 3120a}) - 1] \times 1000$. Duplicate measurements of NIST SRM3120a yielded an average $\delta^{74}Ge$ value of 0.00 ± 0.10‰ (2σ, n = 282) (Fig. S1a), indicating a long-term reproducibility of about ±0.10‰ (2σ). Repeated analyses of Spex and Merck standard solutions yielded an average $\delta^{74}Ge$ value of − 0.69 ± 0.10‰ (2σ, n = 39) and −0.33 ± 0.09‰ (2σ, n = 21), respectively. There are no differences between the measured $\delta^{74}Ge$ values for pure Spex and Merck standard solutions and that for the treated Spex and Merck standard solutions (which underwent the whole sample dissolution and chemical purification procedures), indicating that the total procedure blanks are very low and thus have no contribution to the measured $\delta^{74}Ge$ values (Fig. S1b and c). The measured $\delta^{74}Ge$ values for geochemical reference materials BHVO-2 (basalt), BCR-2 (basalt) and GSR-1 (granite) are 0.57 ± 0.09‰ (2σ, n = 2), 0.55 ± 0.14‰ (2σ, n = 2) and 0.66 ± 0.13‰ (2σ, n = 2), respectively. These values agree with the previously reported average values for standard solutions and reference rocks within analytical uncertainty (e.g., −0.70 ± 0.19‰ (2σ) (Spex) and −0.36 ± 0.08‰ (2σ) (Merck); Qi et al., 2011; Escoube et al., 2012; Meng et al., 2015; Rouxel and Luais, 2017).

3.4. Recovery of Ge during chemical purification

The recovery of Ge during the whole dissolution and chemical purification procedures was estimated by the standard-addition method (Rouxel et al., 2006; Tipper et al., 2008; Meng et al., 2015). About 50 mg powders of standard soil samples (GSS-4 and GSS-7) were doped with various amounts (0–400 ng) of Spex Ge, then these composite samples were dissolved and purified following the above-mentioned procedures. The measured Ge concentrations were positively correlated with the amounts of Ge added into these composite samples, and the regression coefficients and intercepts correspond to the recovery of Ge and the initial concentrations of standard soil samples, respectively. The calculated recoveries of Ge for GSS-4 and GSS-7 after AG1-X8 and AG50W-X8 resin purification range from 93.7% to 99.7% (Fig. S2). The certified initial concentrations of GSS-4 and GSS-7 are 2.04 ± 0.06 (1σ) ppm and 1.70 ± 0.03 (1σ) ppm (n = 4), respectively. Repeat analyses of soil (GSS-4 and GSS-7) and rock (GSR-1, BHVO-2 and BCR-2) standards (up to 200 mg) indicate around 96.6% to 105% of Ge recoveries (based on the recommended Ge concentrations of these standards), and there is no significant change of Ge recoveries with increasing sample weight. The Ge concentrations in the final 4 ml purified solutions of soil and silicate rocks (sample weight: about 100 mg) are around 14.9–28.0 ppb. Sufficient amounts of Ge (>15 ng; Rouxel et al., 2006) can be ensured for routine Ge isotope analyses with a sample weight of about 100 mg.

3.5. Elution of matrix elements during chemical purification

Behaviors of possible matrix elements during the chemical purification for the soil standards (GSS-4 and GSS-7) were checked by using sufficient HF and HNO_3 to elute the columns and analysis of all filtrates and eluant during the uploading and elution of anion/cation-exchange chromatographic column. Large amount of Fe and Mn, alkali and alkaline earth metals (e.g., Ca, Mg, Rb, Sr, Cs and Ba), transition metals (e.g., Cu, Zn, Ni, Sc) were separated mainly during the uploading and elution of AG1-X8 resin by 1 N HF and Milli-Q water. Small proportion of these elements, as well as the other elements (e.g., P, REE, U, Th, Pb and V), were eluted during the recovery of Ge by 12 ml 3 N HNO_3. The residual of above elements can be further separated from Ge during the uploading and elution of AG50-X8 resin (Table S1). High field strength elements (HFSEs: e.g., Nb, Ta, Zr, Hf and Ti) follow Ge closely during the uploading and elution of AG1-X8 resin, some of which strongly adsorbed on the AG50W-X8 resin and were separated from Ge during the elution of 0.28 N HNO_3. However, they can be generated or eluted from the AG50W-X8 resin by 3 N HNO_3. The concentrations of possible matrix elements in the final Ge-bearing solutions increase with increasing sample weight (from 50 mg to 200 mg). During the chemical purification processes of soil, saprolite and basalt samples from the Hainan Island, high field strength elements (HFSE, e.g., Nb, Ta, Zr, Hf and Ti) were eluted also at the stage of uploading 4 ml Ge-bearing solutions in 3 N HNO_3 media, and Ge-bearing solutions have suffered distinct Ti and Zr contamination by the former used AG50W-X8 resin (Table S2). Using more concentrated HNO_3 media to wash the AG50W-X8 resin before uploading may help to suppress the HFSE contamination (Rouxel et al., 2006).

3.6. Matrix effect evaluation and possible Ge isotope fractionation during chemical purification

After dissolution and purification, minor Ti, Zr, Nb, Hf and Sn still remained in the Ge-bearing (14.9–28.0 ppb Ge) solutions, with their maximum concentrations being up to 20.6 ppm (Ti), 3.19 ppm (Zr), 93.2 ppb (Nb), 81.7 ppb (Hf) and 16.8 ppb (Sn). The matrix effect or possible influence of these elements on Ge isotope analyses (determined by HG-MC-ICP-MS) were investigated by comparing the Ge isotope composition of the Spex standard solution and that of 10 ppb Spex standard solution doped with

various amounts of these elements. Matrix element/Ge concentration ratios (ppb/ppb) are defined and overlapped the measured corresponding ratios of the eluant after purification of soil, saprolite and basalt samples from the Hainan Island. The δ^{74}Ge values of these composite samples range from -0.77 ± 0.10‰ (2σ) to -0.65 ± 0.10‰ (2σ), indistinguishable from the reported (-0.70 ± 0.11‰ (2σ); Qi et al., 2011; -0.70 ± 0.19‰ (2σ); Meng et al., 2015) or certified values (-0.69 ± 0.10‰ (2σ); this study) of pure Spex standard solution within analytical uncertainty (Table S3, Fig. S3). These facts and results of Meng et al. (2015) indicate that the addition of minor quantity of Ti, Zr, Nb, Hf and Sn into Ge-bearing solutions has no influence on Ge isotope analyses (determined by HG-MC-ICP-MS).

The possible Ge isotope fractionation during the dissolution and chemical purification processes of the soil samples was evaluated by analysis of Ge isotope compositions of composite samples obtained by standard-addition method for Ge recovery. The δ^{74}Ge values of the composite samples (GSS-4 and GSS-7 doped with various amounts of Spex solution) and the percentage of Ge added in these composite samples strictly follow the predicted mixing line between GSS-4 or GSS-7 and Spex standard solution. The calculated δ^{74}Ge values for GSS-4 (0.33‰) and GSS-7 (0.34‰) are indistinguishable (within analytical error) from the duplicate measured values, e.g., 0.32 ± 0.10‰ and 0.33 ± 0.10‰ for GSS-7 (avg. 0.33 ± 0.10‰, n = 2), and 0.32 ± 0.20‰ and 0.30 ± 0.10‰ for GSS-4 (avg. 0.31 ± 0.10‰, n = 2) (Fig. S4). This suggests negligible Ge isotope fractionation during the whole purification and analyses process.

3.7. Element mobility and mass balance calculation

The net gain and loss of a particular element (j) relative to the fresh parent rocks can be expressed as:

$$\tau_{i,j} = \frac{C_{j,w}}{C_{j,p}} \times \frac{C_{i,p}}{C_{i,w}} - 1 \quad (1)$$

where $C_{j,w}$ and $C_{j,p}$ are the concentrations of element j in the weathered soil and fresh parent rock, respectively, and $C_{i,w}$ and $C_{i,p}$ are the concentrations of the relatively most stable element (i) in the weathered soil and fresh parent rock, respectively (e.g., Kurtz et al., 2000, 2002; Lugolobi et al., 2010; Jiang et al., 2018). An element-mass-transfer coefficient $\tau_{i,j} < 0$ would reflect a net loss of element j relative to the parent rock, and vice versa for $\tau_{i,j} > 0$. $\tau_{i,j} = 0$ would indicate that element j is stable and immobile. According to Kurtz et al. (2000, 2002) and Jiang et al. (2018), Nb was chosen as the most stable or reference element i in the mass balance calculation here. The average basaltic elemental concentrations and Nb concentration were adopted for the $C_{j,p}$ and $C_{i,p}$ of the fresh basaltic parent rocks, respectively.

The $\delta^{74}Ge_D$ and Ge/Si_D signatures released or dissolved in soil solutions along depth during progressing weathering of soil and saprolite or extreme weathering of basalts can be evaluated using the following mass balance equations (modified from Lugolobi et al., 2010; Delvigne et al., 2016; Supplement C) postulating that all the elements loss were released into the soil solution:

$$\delta^{74}Ge_{dissolved} = \frac{\delta^{74}Ge_{reactant} - \left(\delta^{74}Ge_{product}(1+\tau_{Ge})\right)}{-\tau_{Ge}} \quad (2)$$

$$Ge/Si_{dissolved} = \frac{Ge/Si_{reactant} - \left(Ge/Si_{product}(1+\tau_{Si})\right)}{-\tau_{Si}} \quad (3)$$

where τ_{Si} and τ_{Ge}, respectively, represent the fractions of Si and Ge loss of the solid weathering products (product), relative to the parent basalts (reactant) during the extreme weathering process.

4. RESULTS

4.1. Germanium and Si concentrations

The soil and saprolite samples contain higher Ge concentrations (2.19–4.12 ppm, avg. 2.93 ppm, n = 52) than the semi-weathered basalt (2.61 ppm) and fresh basalt (1.50–1.73 ppm, avg 1.64 ppm, n = 5). The lowest Ge concentration (i.e., strongest depletion: 2.19 ppm, $\tau_{Ge} = -0.39$) occurs at the soil-saprolite interface, while the highest concentration (i.e., strongest enrichment: 4.12 ppm, $\tau_{Ge} = -0.39$) occurs around the rock-regolith interface. The SiO_2 contents (13.3–42.7%) of the soil and saprolite samples, which are distinctly lower than those (~51%) of fresh basalts, decrease progressively from the bottom to the top of the profile, while the minimum content (the strongest depletion) occurs at soil-saprolite interface (Table 1; Fig. 2).

4.2. Ge/Si ratio

The Ge/Si ratios of soil and saprolite samples range from 5.55 to 13.67 μmol/mol, and slightly decrease from the top (7.49 μmol/mol) to the bottom (5.55 μmol/mol, at ~14 m deep) of the profile. The maximum value (13.67 μmol/mol) occurs at the soil-saprolite interface, and the higher values (~10 μmol/mol) occur near the rock-regolith interface (Fig. 2). Both the semi-weathered basalt (Ge/Si = 5.06 μmol/mol) and fresh basalts exhibit lower Ge/Si ratios than those of the soil and saprolite samples. Ge/Si ratios of the fresh basalts range from 2.43 to 2.80 μmol/mol (avg. 2.66 μmol/mol, n = 5), similar to those of (Hawaiian) basalts (2.3–2.8 μmol/mol, avg. 2.6 μmol/mol; DeArgollo and Schilling, 1978; 2.4 μmol/mol; Rouxel and Luais, 2017).

4.3. Germanium isotopes

The δ^{74}Ge values of the soil and saprolite samples (-0.03 ± 0.10‰ to 0.65 ± 0.10‰) exhibit complex fluctuations with depth. Except for the distinctly low value (0.02 ± 0.10‰) at the soil-saprolite interface, the δ^{74}Ge values generally increase from the top (0.14 ± 0.11‰) to ~4.4 m deep (0.65 ± 0.10‰), and then decrease to ~8 m deep (0.25 ± 0.11‰). After that, the values fluctuate and drop to the minimum (-0.03 ± 0.10‰) at 14.04 m deep, and then eventually increase again to 0.63 ± 0.14‰ near the rock-regolith interface (Fig. 2). The semi-weathered basalt

Table 1
Selected major and trace element concentration, $\delta^{74}Ge$, and other geochemical parameters for the Wenchang basalt weathering profile, South China.

Sample ID	Sample Type	Horizon	Depth (m)	SiO_2 (%)	Fe_2O_3 (%)	Al_2O_3 (%)	MnO (%)	P_2O_5 (%)	Nb (ppm)	Ge (ppm)	pH	CIA[a] (%)	IOL[b] (%)	τ_{Si}	τ_{Ge}	Ge/Si (μmol/mol)	$\delta^{74}Ge$ (‰)	2 σ	Ge/Si_D[c] (μmol/mol)	$\delta^{74}Ge_D$[c] (‰)	$\Delta_{solid\text{-}dissol}$[d] (‰)
WC-1	Soil	A	0.1	29.5	22.2	26.1	0.14	0.42	58.0	2.67	5.07	99.4	62	−0.76	−0.34	7.49	0.14	0.11	1.17	1.33	−1.19
WC-2	Soil	A	0.3	29.9	22.9	26.5	0.18	0.25	57.3	2.69	4.77	99.8	62	−0.76	−0.32	7.44	0.11	0.10	1.14	1.44	−1.33
WC-3	Soil	A	0.5	30.5	22.5	27.0	0.19	0.22	52.2	2.80	4.69	99.9	62	−0.73	−0.23	7.59	0.18	0.10	0.83	1.77	−1.59
WC-4	Soil	A	0.7	30.3	22.5	26.9	0.18	0.22	53.4	2.62	4.67	99.9	62	−0.74	−0.29	7.15	0.14	0.10	1.06	1.51	−1.37
WC-5	Soil	A	0.9	30.6	22.6	27.3	0.20	0.22	51.6	2.59	4.74	99.9	62	−0.73	−0.28	7.00	0.18	0.10	1.02	1.48	−1.30
WC-6	Soil	A	1.1	30.9	22.4	27.8	0.21	0.22	48.4	2.96	4.65	99.9	62	−0.70	−0.12	7.92	0.11	0.10	0.45	3.73	−3.62
WC-7	Soil	A	1.3	27.7	24.2	28.6	0.19	0.25	43.4	2.86	4.70	99.8	66	−0.70	−0.05	8.54	0.17	0.11	0.19	7.50	−7.33
WC-8	Soil	A	1.5	32.1	21.6	28.0	0.16	0.21	42.3	2.98	4.83	99.9	61	−0.65	0.02	7.68	0.18	0.10	−0.06	−23.6	23.8
WC-9	Soil	A	1.7	32.3	21.7	27.9	0.14	0.22	42.3	3.22	4.87	99.9	61	−0.65	0.10	8.25	0.24	0.13	−0.40	−2.86	3.10
WC-10	Soil	A	1.9	32.0	21.6	27.7	0.16	0.22	40.8	2.82	4.92	99.9	61	−0.64	−0.004	7.29	0.28	0.10	0.02	64.2	−63.9
WC-11	Soil	A	2.1	30.9	22.7	27.5	0.19	0.36	41.4	3.10	4.98	99.8	62	−0.65	0.08	8.30	0.39	0.11	−0.32	−1.51	1.90
WC-12	Soil	A	2.4	13.3	28.5	32.3	0.13	0.64	51.8	2.19	5.03	99.9	82	−0.88	−0.39	13.67	0.02	0.10	1.18	1.35	−1.33
WC-13	Saprolite	B	2.8	32.4	20.9	28.3	0.38	0.34	36.1	2.81	5.06	99.9	60	−0.58	0.12	7.17	0.49	0.10	−0.55	0.08	0.41
WC-14	Saprolite	B	3.1	32.3	22.3	27.0	0.21	0.25	40.7	3.11	5.08	99.9	60	−0.63	0.10	7.96	0.42	0.10	−0.43	−0.77	1.19
WC-15	Saprolite	B	3.5	34.2	19.6	27.9	0.43	0.20	38.5	3.29	5.01	99.9	58	−0.59	0.23	7.96	0.56	0.10	−1.05	0.65	−0.09
WC-16	Saprolite	B	3.9	32.6	22.2	26.8	0.31	0.24	52.1	3.19	4.96	99.8	60	−0.71	−0.12	8.09	0.56	0.10	0.44	0.39	0.17
WC-17	Saprolite	B	4.4	33.3	22.3	27.0	0.19	0.23	49.6	2.88	4.92	99.9	60	−0.69	−0.16	7.15	0.65	0.10	0.63	−0.02	0.67
WC-18	Saprolite	B	4.9	35.8	17.2	29.3	0.13	0.20	36.8	2.81	4.81	100	57	−0.55	0.10	6.49	0.62	0.10	−0.49	1.42	−0.80
WC-19	Saprolite	B	5.3	33.4	20.2	28.1	0.23	0.34	38.9	2.41	4.84	100	59	−0.60	−0.11	5.97	0.51	0.10	0.47	0.79	−0.28
WC-20	Saprolite	B	5.7	33.2	21.1	27.5	0.23	0.24	39.2	2.65	4.74	99.9	59	−0.61	−0.03	6.60	0.62	0.10	0.11	−2.47	3.09
WC-21	Saprolite	B	6.1	32.4	20.1	27.5	1.82	0.25	36.9	2.50	4.81	99.9	60	−0.59	−0.02	6.38	0.53	0.10	0.11	0.95	−0.42
WC-22	Saprolite	B	6.7	34.5	19.1	28.2	0.47	0.19	37.3	3.02	4.71	99.9	58	−0.57	0.17	7.24	0.45	0.10	−0.78	−0.09	0.54
WC-23	Saprolite	B	7.1	34.8	18.6	28.4	0.32	0.25	43.9	3.19	4.75	99.9	57	−0.63	0.05	7.58	0.46	0.11	−0.20	−1.24	1.70
WC-24	Saprolite	B	7.3	33.3	21.3	27.2	0.29	0.19	47.1	3.29	4.75	99.9	59	−0.67	0.01	8.17	0.41	0.10	−0.03	−19.6	20.0
WC-25	Saprolite	B	7.5	33.9	21.9	27.2	0.19	0.16	47.1	3.14	4.77	99.9	59	−0.67	−0.04	7.66	0.25	0.10	0.16	7.61	−7.36
WC-26	Saprolite	B	8.0	33.6	21.4	27.0	0.28	0.18	45.5	2.56	4.81	99.9	59	−0.66	−0.19	6.30	0.25	0.11	0.77	1.78	−1.53
WC-27	Saprolite	B	8.4	33.2	22.6	26.6	0.21	0.16	46.0	3.23	4.77	99.9	60	−0.67	0.01	8.05	0.35	0.10	−0.05	−15. 8	16.1
WC-28	Saprolite	B	8.6	32.5	24.2	26.0	0.29	0.17	47.5	3.54	4.75	99.9	61	−0.68	0.07	9.01	0.62	0.10	−0.29	1.70	−1.08
WC-29	Saprolite	B	8.8	34.4	21.5	27.1	0.19	0.14	47.7	3.51	4.74	99.8	59	−0.67	0.06	8.44	0.56	0.10	−0.24	0.89	−0.33
WC-30	Saprolite	B	9.1	34.5	21.1	27.3	0.23	0.14	39.8	2.94	4.79	99.9	58	−0.60	0.06	7.05	0.33	0.10	−0.29	−2.93	3.26
WC-31	Saprolite	B	9.28	34.7	21.1	27.3	0.20	0.13	43.4	2.93	4.85	99.9	58	−0.63	−0.03	6.98	0.51	0.10	0.11	1.61	−1.10
WC-32	Saprolite	B	9.56	34.7	21.2	27.2	0.24	0.12	45.8	3.08	4.82	99.7	58	−0.65	−0.03	7.34	0.46	0.13	0.13	3.04	−2.58
WC-33	Saprolite	B	9.84	34.8	20.6	27.4	0.28	0.12	42.7	2.70	4.87	99.9	58	−0.62	−0.09	6.42	0.20	0.10	0.38	4.03	−3.83
WC-34	Saprolite	B	10.12	34.2	21.9	26.9	0.38	0.12	42.3	2.73	4.94	99.8	59	−0.63	−0.07	6.60	0.23	0.10	0.30	4.66	−4.43
WC-35	Saprolite	B	10.40	33.7	23.0	26.4	0.40	0.14	42.8	2.98	4.93	99.9	59	−0.64	0.003	7.31	0.42	0.10	−0.01	−36.4	36.8
WC-36	Saprolite	B	10.68	34.5	21.7	27.0	0.26	0.10	40.9	2.69	4.93	99.9	59	−0.61	−0.05	6.45	0.29	0.10	0.23	5.07	−4.78
WC-37	Saprolite	B	10.96	34.6	21.6	27.0	0.27	0.10	39.1	2.71	4.97	99.9	58	−0.59	−0.001	6.48	0.34	0.10	0.01	154	−154
WC-38	Saprolite	B	11.24	34.6	20.7	26.8	0.28	0.21	43.6	2.83	5.00	99.9	58	−0.63	−0.07	6.77	0.25	0.16	0.27	4.73	−4.48
WC-39	Saprolite	B	11.52	33.6	22.0	26.2	0.33	0.36	47.4	3.25	5.00	99.9	59	−0.67	−0.01	8.00	0.27	0.10	0.05	22.7	−22.5
WC-40	Saprolite	B	11.80	34.4	21.5	26.6	0.27	0.14	40.3	2.80	5.01	99.9	58	−0.61	0.001	6.73	0.33	0.20	−0.01	−184	184
WC-41	Saprolite	B	12.08	34.1	21.4	26.9	0.37	0.21	42.6	3.07	4.98	99.9	59	−0.63	0.04	7.45	0.20	0.10	−0.16	−8.65	8.85
WC-42	Saprolite	B	12.36	34.9	21.2	26.5	0.28	0.09	38.5	2.65	5.24	99.7	58	−0.58	−0.01	6.28	0.29	0.10	0.04	30.8	−30.5

WC-43	Saprolite	B	12.64	35.6	20.2	26.9	0.26	0.08	35.6	3.17	5.43	99.7	57	−0.54	0.28	7.37	0.52	0.10	−1.41	0.45	0.07
WC-44	Saprolite	B	12.92	34.0	22.1	26.2	0.57	0.15	44.5	2.92	5.29	99.8	59	−0.65	−0.06	7.10	0.43	0.10	0.22	2.45	−2.02
WC-45	Saprolite	B	13.20	34.1	21.5	26.5	0.26	0.16	43.4	2.69	5.28	99.9	58	−0.64	−0.11	6.53	0.32	0.10	0.45	2.38	−2.06
WC-46	Saprolite	B	13.48	35.0	19.7	26.6	0.28	0.26	39.7	2.37	5.47	99.9	57	−0.59	−0.14	5.60	0.18	0.10	0.63	2.76	−2.58
WC-47	Saprolite	B	13.76	34.0	21.3	26.1	0.30	0.37	40.7	2.54	5.58	99.8	58	−0.61	−0.10	6.18	0.13	0.10	0.44	4.20	−4.07
WC-48	Saprolite	B	14.04	35.5	19.7	26.5	0.33	0.36	35.9	2.38	5.55	99.7	57	−0.54	−0.05	5.55	−0.03	0.10	0.22	12.7	−12.7
WC-49	Saprolite	B	14.32	33.4	21.1	26.1	0.27	0.56	39.4	2.45	5.95	99.8	59	−0.61	−0.10	6.07	0.52	0.10	0.46	0.71	−0.19
WC-50	Saprolite	B	14.60	34.7	20.9	25.1	0.44	0.62	38.0	3.88	6.05	99.7	57	−0.58	0.47	9.25	0.63	0.10	−2.17	0.82	−0.19
WC-51	Saprolite	B	14.88	35.6	20.5	24.1	0.14	0.62	45.2	4.12	6.07	99.7	56	−0.64	0.31	9.57	0.55	0.10	−1.31	0.58	−0.03
WC-52	Saprolite	B	15.16	37.5	18.1	24.9	0.28	0.42	35.7	3.71	6.05	99.7	53	−0.51	0.50	8.18	0.40	0.10	−2.58	0.12	0.28
WC-53	SWB[e]	C	15.28	42.7	14.8	18.8	0.12	0.57	31.4	2.61	5.84	69.1	44	−0.37	0.20	5.06	0.57	0.10	−1.42	0.72	−0.15
WC-54	Basalt	R	15.83	51.4	11.0	14.2	0.12	0.32	24.7	1.65		40.3	33	−0.04	−0.04	2.66	0.54	0.10			
WC-55	Basalt	R	16.43	51.4	11.3	14.1	0.17	0.33	23.9	1.65		40.1	33	0.00	−0.01	2.66	0.32	0.10			
WC-56	Basalt	R	17.43	50.2	11.7	13.9	0.13	0.32	22.9	1.68		40.9	34	0.02	0.06	2.77	0.45	0.10			
WC-57	Basalt	R	18.73	51.1	11.5	14.1	0.15	0.32	24.4	1.73		40.4	33	−0.03	0.02	2.80	0.55	0.10			
WC-58	Basalt	R	19.73	51.1	11.5	14.1	0.15	0.32	22.4	1.50		40.5	33	0.06	−0.04	2.43	0.54	0.10			

[a] CIA = $Al_2O_3/(Al_2O_3 + CaO^* + Na_2O + K_2O) * 100$ (moles%, Nesbitt and Young, 1982), $CaO^* = CaO - (10/3 * P_2O_5)$ (McLennan, 1993).

[b] IOL = $(Al_2O_3 + Fe_2O_3)/(SiO_2 + Al_2O_3 + Fe_2O_3) * 100$ (wt.%, Babechuk et al., 2014).

[c] The calculated δ^{74}Ge and Ge/Si signatures released in soil solutions based on mass balance calculation.

[d] The estimated fractionation factor ($\Delta_{solid\text{-}dissolved} = 1000 * Ln(\alpha)$).

[e] SWB = Semi-weathered basalt. The CIA (nearly 100%) and IOL (about 60% to 82%) values indicate an extreme (Nesbitt and Wilson, 1992) or weakly to moderately lateritized (Babechuk et al., 2014) weathering of soils and saprolites from this profile.

(WC-53) has δ^{74}Ge value of 0.57 ± 0.10‰, which is basically similar to those of fresh basalts. Three basalt samples exhibit homogeneous Ge isotope composition ($\delta^{74}Ge = 0.54 \pm 0.10$‰ ($2\sigma$), $n = 3$), while the other two basalt samples show lighter Ge isotope compositions (0.32 ± 0.10‰ and 0.45 ± 0.10‰) than the average bulk silicate earth (BSE) value ($\delta^{74}Ge = 0.59 \pm 0.18$‰; Escoube et al., 2012; $\delta^{74}Ge = 0.58 \pm 0.21$‰; Rouxel and Luais, 2017).

5. DISCUSSION

5.1. Long-term Ge/Si and Ge isotope fractionation during basalt-saprolite and saprolite-soil transformation

Elemental behaviors (leaching and redistribution) of Si and Ge in the weathering profiles are not only related to climate, weathering duration and parent rock type, but also related to the profile architecture (various combinations of different horizons) and depth. For example, Kurtz et al. (2002) found that the youngest basaltic chronosequence soils from the Hawaiian Islands have Ge/Si ratios of 2.7–3.0 μmol/mol (τ_{Si}, τ_{Ge} near 0), whereas the older soils have highly fractionated Ge/Si ratios (5.5–24.3 μmol/mol, $\tau_{Si} = -0.8$ to -1, $\tau_{Ge} = -0.8$ to 0.10), some soil horizons in these thin profiles (thickness < 1.20 m) show as much as 80% Si loss, without any apparent net loss of Ge. Lugolobi et al. (2010) observed that the soil Ge/Si ratios (1.1–1.6 μmol/mol) are lower than those (1.8–1.6 μmol/mol) of saprolites from a quartz diorite weathering profile (thickness: 7.35 m) in Puerto Rico. Moreover, both Si and Ge in this profile are distinctly leached ($\tau_{Si} = -0.87$ to -0.07, $\tau_{Ge} = -0.70$ to -0.03, Zr as reference element; Lugolobi et al., 2010).

The Wenchang weathering profile is very thick (~15 m), and is dominated by relatively homogeneous saprolite with an extremely thin saprolite-bedrock transition. Our results indicate that Si was continuously leached ($\tau_{Si} = -0.88$ to -0.37) out from the profile, whereas Ge shows distinct depletion ($\tau_{Ge} = -0.35$ to -0.05, above 1.3 m deep), internal redistribution (alternative enrichment and depletion from 1.5 m to 15.28 m deep) and local-scale enrichment ($\tau_{Ge} = 0.23$–0.50 near the soil-saprolite and saprolite-bedrock interfaces, respectively) along depth. The semi-weathered basalt exhibits the minimum Si loss ($\tau_{Si} = -0.37$) and distinct Ge enrichment ($\tau_{Ge} = 0.20$). The enhanced Ge/Si ratio (5.06 μmol/mol) and Ge enrichment of this sample may be overprinted by the progressive weathering of saprolites (Section 5.3). Therefore, we calculated the average compositions of soil, saprolite and basalts, respectively, and then used the stepwise weathering model (Lugolobi et al., 2010) and mass balance calculation to evaluate the long-term Ge/Si and Ge isotope fractionation trends during the basalt-saprolite and saprolite-soil transformation. In this model, the chemical weathering processes of parent rocks were divided into two steps: (1) gradual transition from bedrock to saprolite via initial weathering, and (2) transition from saprolite to soil via progressive weathering or pedogenesis.

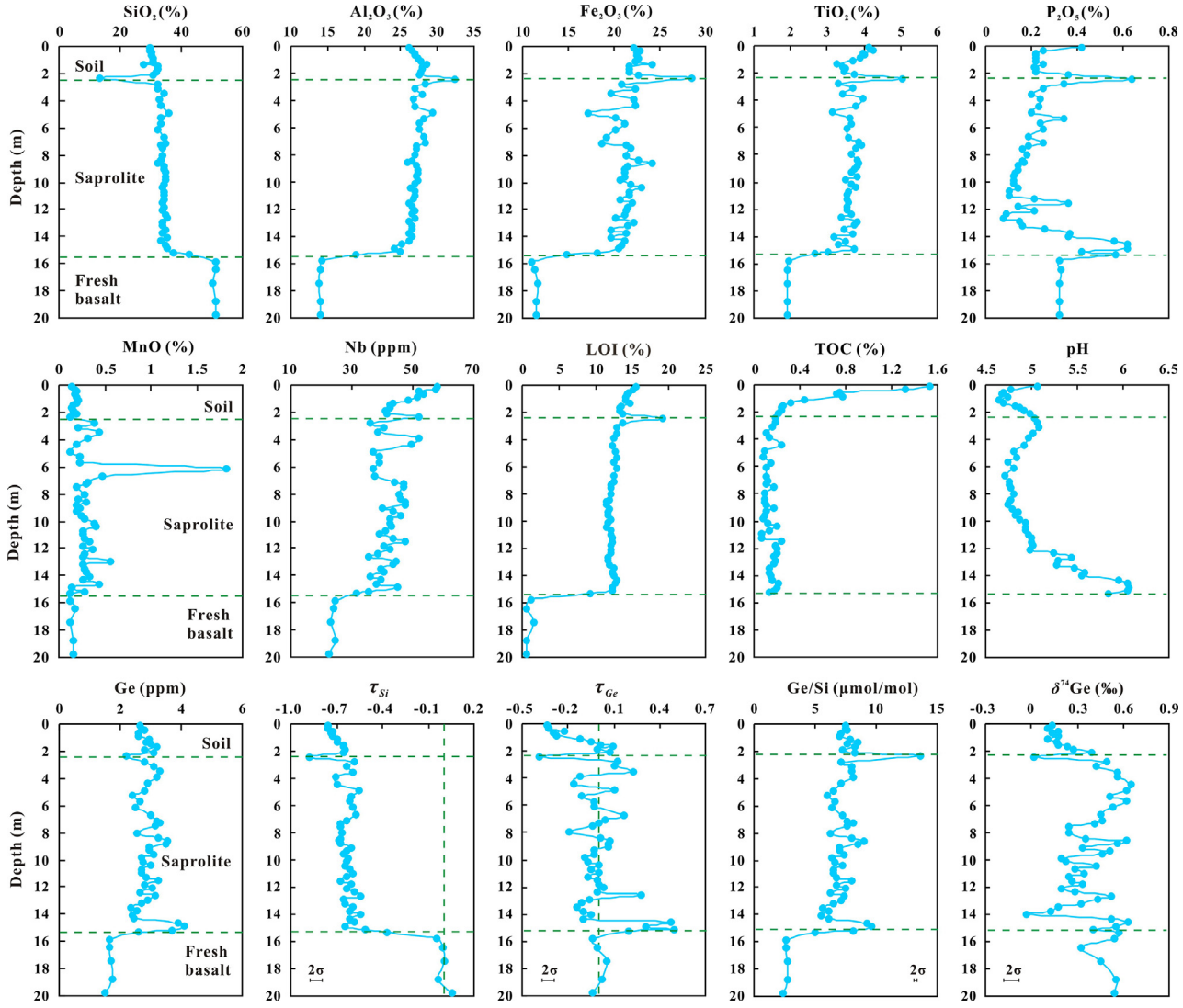

Fig. 2. Germanium concentrations, τ_{Si}, τ_{Ge}, Ge/Si ratios and δ^{74}Ge values across the Wenchang basalt weathering profile. Major element concentrations, LOI values, Nb concentrations, TOC contents, pH values were listed for comparison (data from Jiang et al., 2018). The uncertainties (2σ) for τ_{Si}, τ_{Ge}, Ge/Si ratio and δ^{74}Ge are ±0.08, ±0.08, ±0.29 and ±0.10‰, respectively. The dashed vertical line denotes Tau = 0.

The results indicate that the Ge/Si ratio of solid weathering products tends to increase, while average δ^{74}Ge value tends to decrease from basalt through saprolite to soil (Table 2). A 62% Si loss ($\tau_{Si} = -0.62$) and slight (or no significant) Ge isotope fractionation (δ^{74}Ge changes from 0.54‰ to 0.40‰) are resulted in the basalt-saprolite weathering transformation, while Ge loss in the saprolite is negligible ($\tau_{Ge} = 0.02$). The saprolite-soil transformation involves 26% Si loss ($\tau_{Si} = -0.26$), 17% Ge loss ($\tau_{Ge} = -0.17$) and significant Ge isotope fractionation (δ^{74}Ge changes from 0.40‰ to 0.19‰). These data for basalt-saprolite weathering transformation should be interpreted with caution. The distinct internal redistribution and local enrichment of Ge along depth of the Wenchang weathering profile is possibly resulted from progressive weathering or pedogenetic processes. Generally, the Wenchang basalt weathering profile exhibits higher Si loss and lower Ge loss than those of the Luquillo quartz diorite weathering profile. The latter has been attributed to the incongruent weathering of plagioclase and hornblende, and retention of primary igneous quartz (with a low Ge/Si ratio) during the diorite weathering processes (Lugolobi et al., 2010).

5.2. Ge/Si fractionation in soils and saprolites

Plants are known to discriminate against Ge during nutrient uptake (Derry et al., 2005; Lugolobi et al., 2010; Meek et al., 2016). Retention of Ge by soil organic matter is unlikely an important mechanism for Ge/Si fractionation in Hawaiian soils (Kurtz et al., 2002). Sequestration of Ge by secondary aluminosilicate (or clay) minerals (e.g., kaolinite) or soil silicates were regarded as the dominant Ge/Si fractionation mechanism for solid weathering products (e.g., soil, saprolite and paleosol) (Mortlock and

Table 2
Comparisons of stepwise elemental loss during basalt and diorite weathering.

	n	SiO_2 (wt%)	1σ	Ge (ppm)	1σ	Nb(ppm)	1σ	Ge/Si_S[a] (μmol/mol)	1σ	$\delta^{74}Ge_S$[a] (‰)	1σ	Weathering step	τ_{Si}	1σ	τ_{Ge}	1σ	Ge/Si_D[a] (μmol/mol)	1σ	$\delta^{74}Ge_D$[a](‰)	1σ
Wenchang basalt weathering profile (15.28 m deep)																				
Average soil[b]	11	30.6	1.3	2.85	0.20	48.3	6.5	7.70	0.50	0.19	0.08	Saprolite → soil	−0.26	0.05	−0.17	0.04	5.41	1.68	1.43	0.96
Average saprolite	40	34.2	1.1	2.97	0.41	42.0	4.2	7.19	0.96	0.40	0.16	Basalt → saprolite	−0.62	0.07	0.02	0.004	0.12[c]	0.03	7.40[c]	3.63
Average basalt	5	51.0	0.5	1.64	0.09	23.7	1.0	2.66	0.15	0.54[d]	0.01									
Luquillo (Puerto Rico) quartz diorite weathering profile (7.35 m deep)[e]																				
Average soil	3	77.1		1.3		159[f]		1.4				Saprolite → soil	−0.18		−0.50		6.4			
Average saprolite	30	66.2		1.8		112[f]		2.3				Diorite → saprolite	−0.47		−0.39		1.7			
Quartz diorite		61.8		1.5		56[f]		2.0												

[a] Ge/Si_S and $\delta^{74}Ge_S$ represent the Ge/Si and $\delta^{74}Ge$ of the solid weathering products or parent rocks. The dissolved $\delta^{74}Ge$ and Ge/Si signatures ($\delta^{74}Ge_D$ and Ge/Si_D) for pore water were calculated and based on Eqs. (2) and (3), respectively.

[b] The soil sample WC-12 was excluded for distinct leaching.

[c] The values were approximated at $\tau_{Ge} = -0.02$.

[d] Based on three basalt samples.

[e] Data after Lugolobi et al. (2010).

[f] The reported concentrations for Zr. The uncertainties (1σ) for average compositions were based on statistics of selected samples, those for τ_{Si}, τ_{Ge}, Ge/Si_D and $\delta^{74}Ge_D$ were based on error propagation.

Froelich, 1987; Froelich et al., 1992; Kurtz et al., 2002; Anders et al., 2003; Scribner et al., 2006; Lugolobi et al., 2010; Delvigne et al., 2016). This hypothesis is mainly supported by: (1) the observed Si vs. Ge correlation in solid weathered products (clay minerals and Fe oxides dominant). For example, Kurtz et al. (2002) and Scribner et al. (2006) found positively SiO_2 vs. Ge correlation in the soils developed on basaltic soil chronosequence in the Hawaiian

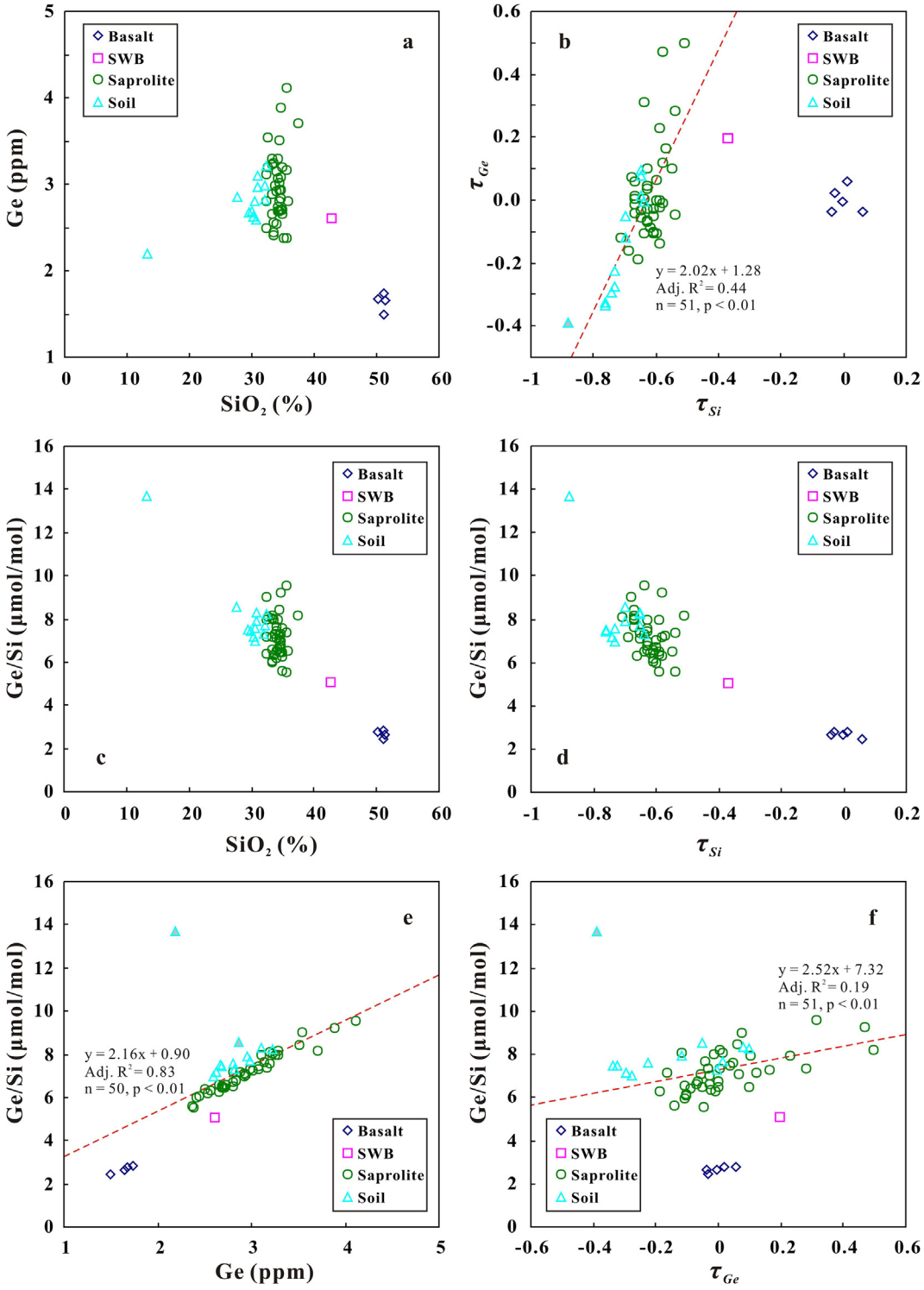

Fig. 3. Scatter diagrams illustrating different behaviors of Ge and Si during extreme weathering of basalts. (a) SiO_2 vs. Ge; (b) τ_{Si} vs. τ_{Ge}; (c) SiO_2 vs. Ge/Si ratio; (d) τ_{Si} vs. Ge/Si ratio; (e) Ge vs. Ge/Si ratio; (f) τ_{Ge} vs. Ge/Si ratio. The filled legends represent that the samples were excluded from the statistics. The adjusted R^2 values were calculated after Baronas et al. (2017b).

Islands. (2) Secondary kaolinite formed by granite weathering contains higher Ge/Si ratios (4.8–6.1 μmol/mol) than those of the parental rocks and saprolites (Kurtz et al., 2002; Lugolobi et al., 2010).

For the Wenchang basalt weathering profile, although secondary kaolinite is the dominant mineral phase in the weathered solid products (Jiang et al., 2018), we noticed that: (1) there are no distinct Ge vs. Si or Ge/Si vs. Si correlations (Fig. 3a and c) for most soil and saprolite samples; (2) the sample (WC-12) with the highest Ge/Si ratio (13.67 μmol/mol) has the strongest Si and Ge depletions (Fig. 3b and d), whose mineral compositions indicate that the maximum degree of hydrolysis of kaolinite and gibbsite formation occurred near the soil-saprolite interface (Jiang et al., 2018); (3) Si has been continuously leached out from the solid weathered products during the entire history (i.e., basalt → semi-weathered basalt → saprolites and soils) (Fig. 3b); (4) Ge shows distinct enrichments (τ_{Ge}: up to 0.50) in the semi-weathered basalt and saprolite samples near the rock-regolith interface. Kurtz et al. (2002) found that the young, incipiently-weathered soils (0.3–2.1Ka) developed on the Hawaiian basalts have lost very little Ge or Si, and have Ge/Si ratios similar to parent material (~2.6 μmol/mol). Therefore, the higher Ge/Si ratio (5.06–9.57 μmol/mol) of these samples indicate that their geochemical signatures have been overprinted by progressive weathering of upper saprolites. (Figs. 2 and 3b); (5) For most of the soil and saprolite samples (except sample WC-12), there are distinct or overall correlations between Ge concentrations (or τ_{Ge} values) and Ge/Si ratios (Fig. 3e and f). This indicates that the Ge/Si changes of in most soil and saprolite samples are mainly controlled by the Ge enrichment/depletion (under the background of continuous Si depletion) during the extreme tropical weathering of the Wenchang basalts.

The soil and saprolite samples from the Wenchang basalt weathering profile are characterized by high Al_2O_3 and Fe_2O_3 concentrations (up to 32.3% and 28.5%, respectively). The mineral assemblage is dominated by kaolinite, Fe-oxides/-hydroxides and gibbsite (or boehmite), indicating extensive desilication and ferrallitic weathering (Jiang et al., 2018). There are no distinct correlations between Ge and Fe_2O_3 (or Al_2O_3) concentrations (Fig. 4a and b), and the sample (WC-12) with the highest Fe_2O_3 and

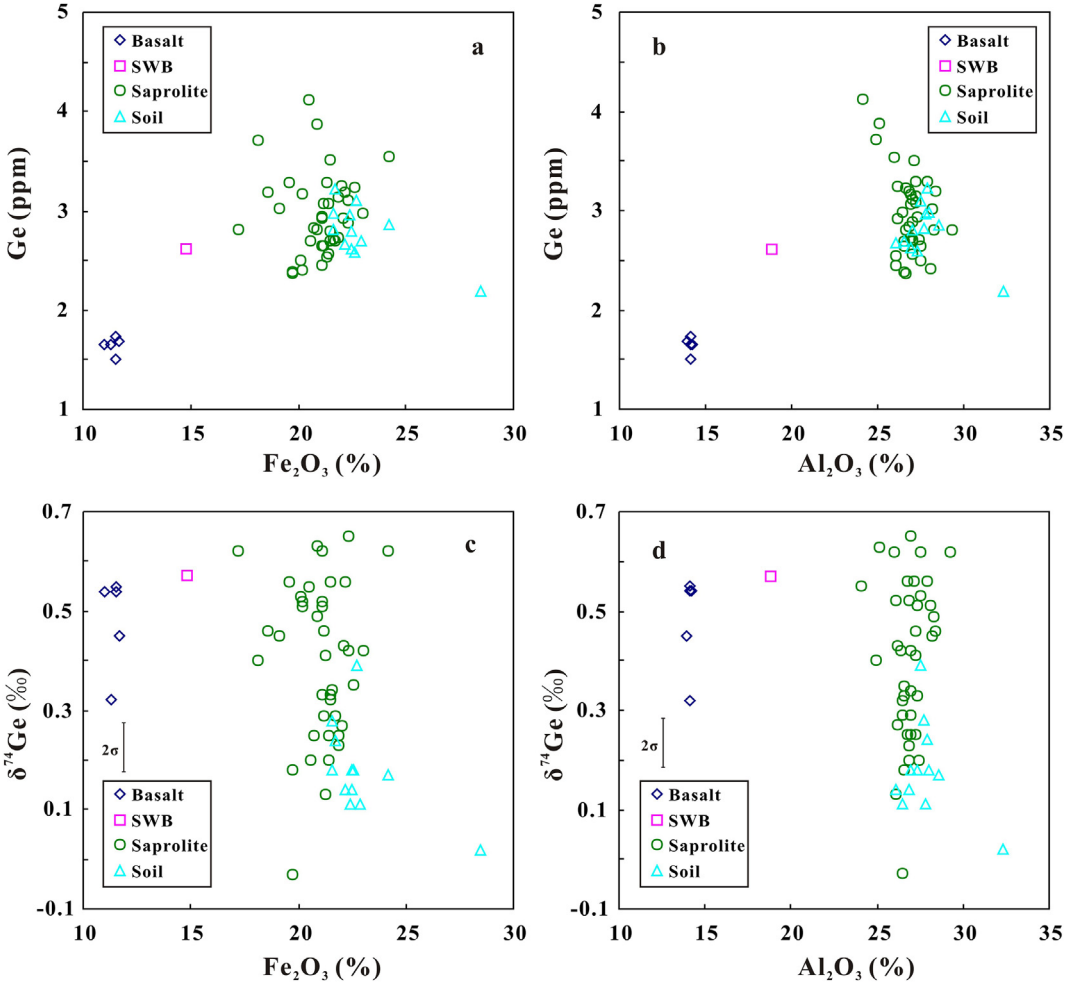

Fig. 4. Scatter diagrams illustrating the behaviors of Ge, Fe, Al and Ge isotope fractionation during extreme weathering of basalts. (a) Fe_2O_3 vs. Ge; (b) Al_2O_3 vs. Ge; (c) Fe_2O_3 vs. $\delta^{74}Ge$; (d) Al_2O_3 vs. $\delta^{74}Ge$.

Al_2O_3 concentrations actually contains the lowest Ge and SiO_2 concentrations. The highest Ge/Si ratio of this sample can be attributed to significant depletion of Si (relative to Ge) during the kaolinite hydrolysis and gibbsite formation processes. Moreover, the Ge/Si ratios of most soil and saprolite samples from Wenchang are distinctly higher than those reported for secondary kaolinite (4.8–6.1 μmol/mol; Kurtz et al., 2002; Lugolobi et al., 2010). Kurtz et al. (2002) and Scribner et al. (2006) found that both Ge and Fe concentrations decrease in the Hawaiian soil samples, indicating that Ge sequestration is independent from the Fe redox behavior, and that precipitation of Fe-oxyhydroxides is not a major factor for Ge/Si fractionation during weathering. Although allophane can incorporate substantial amount of dissolved Ge (Kurtz et al., 2002), it was not found in our soil and saprolite samples.

Published sequential extraction results of eight Hawaiian soil samples demonstrate that Ge concentrations in the AOD (noncrystalline aluminosilicates and Fe-Al sesquioxides), DC (crystalline Fe and Al-sesquioxides), and NaOH (kaolin, opal) extraction phases are distinctly lower than those of bulk soil, while unextractable residual solids generally contain higher Ge concentrations than bulk soil (Kurtz et al., 2002). A more recent sequential extraction study indicated that Ge in two soil samples from Freiberg (Germany) occurs mainly in the residual fractions (80.6–91.8%) and minor in the operationally-defined crystalline Fe/Mn-oxides (3.2–8.3%) (Wiche and Heilmeier, 2016). However, the different vertical distribution patterns of Ge and MnO along depth imply different geochemical behaviors of Ge and Mn under extreme weathering of the Wenchang basalts (Fig. 4). These different experimental results and our results (Figs. 2 and 4) indicate that Fe, Mn and Al-sesquioxides are not the major factors for Ge/Si fractionation or Ge enrichment/depletion, and support that Ge may have been mainly sequestrated by a non-silicate phase during weathering (i.e., Scribner et al., 2006).

5.3. Controls on Ge isotope fractionation during extreme weathering of basalts

Both theoretical calculations and adsorption and coprecipitation experiments indicate that light Ge isotopes are preferentially enriched on the surfaces of Fe-oxyhydroxides ($\Delta^{74}Ge_{\text{Fe-oxide–Solution}} = -1.6$ to -4.4‰) (Li and Liu, 2010; Pokrovsky et al., 2014). Recent studies demonstrated that sorption processes of Fe (hydro)-oxides are the dominant factor for several isotope fractionation systems (e.g., Si, Cr and Mo) during chemical weathering (Wille et al., 2018; Wang et al., 2018). The main lines of geochemical evidence include: (1) Co-variation between Si and Cr isotopes, as well as their co-variations with Ti-normalized iron contents in saprolite samples (Wille et al., 2018); (2) negative Mo content (or τ_{Mo} values) vs. $\delta^{98/95}$Mo correlations in saprolites; and more importantly (3) large proportion (41.5–86.2%) of total Mo with light $\delta^{98/95}$Mo (-1.57‰ to -0.59‰, cf. -0.31‰ of unaltered granites) is associated with Fe (hydro)-oxides (Wang et al., 2018). However, for the Ge elemental and isotope systems, published sequential extraction studies demonstrated that Ge is mainly concentrated in the residual soil fraction (Kurtz et al., 2002; Wiche and Heilmeier, 2016). Our results indicate no significant correlation between δ^{74}Ge and Al_2O_3, Fe_2O_3 and MnO contents for most soil and saprolite samples (Figs. 2, 4c and d). Therefore, the secondary Al-Fe-Mn (hydro)-oxides formed via chemical weathering of basalt are not the main controlling factors for Ge isotope fractionation during extreme weathering of basalts in tropical climate. However, more mineral separation or similar targeted leaching works are needed in the future to locate the chemical association of Ge in solid weathering products.

For the Wenchang basalt weathering profile, δ^{74}Ge values are positively correlated with Ge concentrations, τ_{Ge}, and Ge/Si ratios for most soil and saprolite samples (Fig. 5a–c), which means that the higher-Ge samples tend to have heavier Ge isotopes and higher Ge/Si ratios, and the opposite is true for the samples with higher degree of Ge leaching. This indicates that the variation of Ge concentration and Ge isotope fractionation of these samples can be explained by a unified adsorption/desorption (or enriched/depleted) model. Similar to the silicon isotope in river water (Georg et al., 2007; Hughes et al., 2013) or Ge isotope in Ge-rich coal (Qi et al., 2011), the Ge isotope fractionation during basalt weathering can be ascribed either to a batch equilibrium or a Rayleigh-type model:

Rayleigh:

$$\delta^{74}Ge_D = (1000 + \delta^{74}Ge_B) * f_{Ge}^{(\alpha-1)} - 1000 \quad (4)$$

$$\frac{(1000 + \delta^{74}Ge_S)}{(1000 + \delta^{74}Ge_B)} = \frac{1 - f_{Ge}^{\alpha}}{1 - f_{Ge}} \quad (5)$$

Batch equilibrium:

$$\delta^{74}Ge_D = \delta^{74}Ge_B - \varepsilon(1 - f_{Ge}) \quad (6)$$

$$\delta^{74}Ge_S = \delta^{74}Ge_B + \varepsilon(f_{Ge}) \quad (7)$$

$$\varepsilon = (\delta^{74}Ge_S - \delta^{74}Ge_B)/f_{Ge} \quad (8)$$

where α is the fractionation factor, ε is (1000 * Ln(α)) in permil unit, f_{Ge} is the fraction of Ge remaining in the solution (equal to $Q_{Ge,D}/Q_{Ge,T}$ or $-\tau_{Ge}$, Supplement C), and $\delta^{74}Ge_D$, $\delta^{74}Ge_B$ and $\delta^{74}Ge_S$ are the isotope compositions of the dissolved Ge, of the unweathered basalt and of the accumulated or total solid weathering product (soil and saprolite), respectively.

Relative to the Ge isotope composition of bulk silicate earth (BSE) ($\delta^{74}Ge = 0.59 \pm 0.18$‰; Rouxel et al., 2006; Escoube et al., 2012; Rouxel and Luais, 2017), the lighter Ge isotopes ($\delta^{74}Ge = 0.32 \pm 0.10$‰ and 0.45 ± 0.10‰) of the two basalt samples may be caused by mild weathering or their inherited Ge isotope inhomogeneities, e.g., $\delta^{74}Ge = 0.37 \pm 0.10$‰ for BHVO-1 (Luais, 2012). For the sake of clear comparison, we only selected the average composition ($\delta^{74}Ge = 0.54 \pm 0.10$‰ (2σ)) of the three basalt samples to represent the Ge isotope composition of regional basalts. The generally lighter or similar Ge isotope compositions of the solid weathering product (soil: average $\delta^{74}Ge = 0.19$‰; saprolite: average $\delta^{74}Ge = 0.40$‰) and heavier composition of basalt-draining rivers from Hawaii ($\delta^{74}Ge = 2.33$–3.63‰, Baronas et al., 2017a), relative to

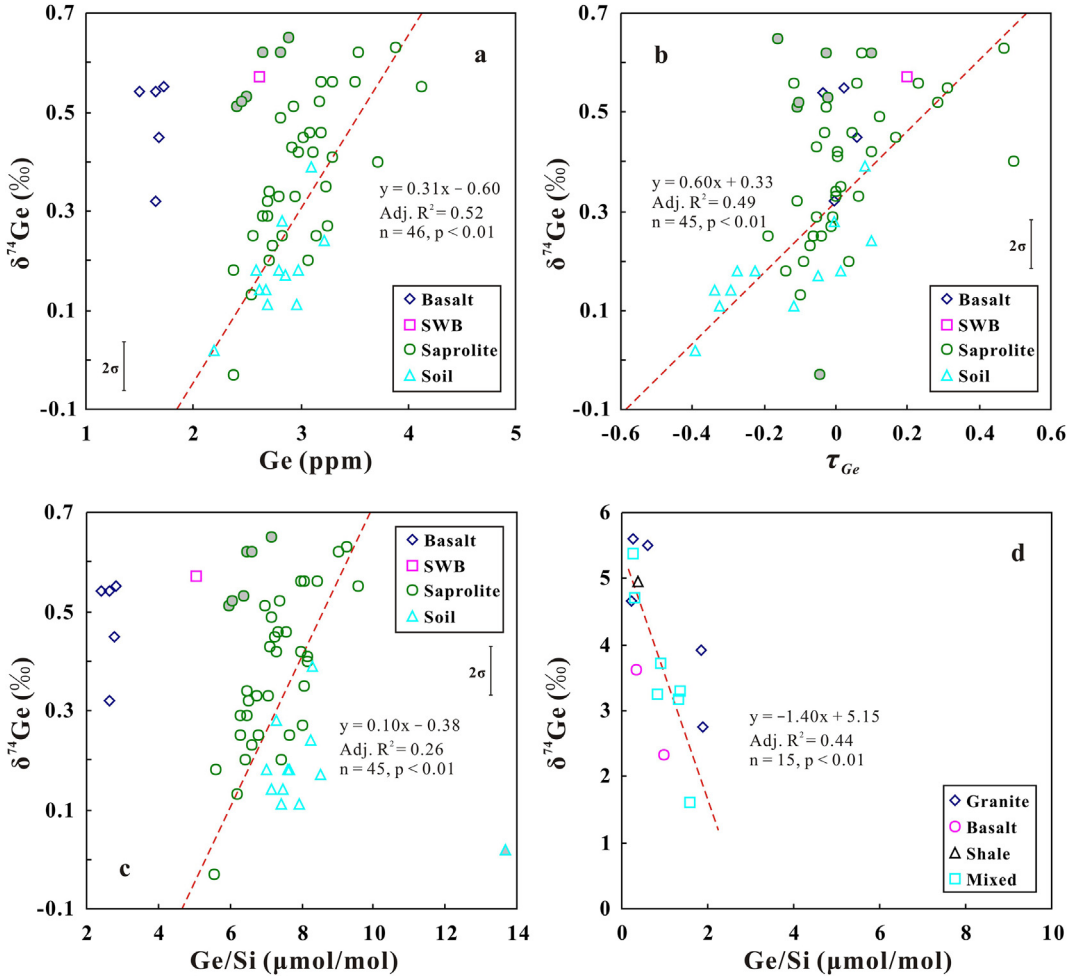

Fig. 5. Scatter diagrams illustrating the behaviors of Ge content, Ge isotope and Ge/Si fractionation during weathering processes. (a) Ge vs. δ^{74}Ge; (b) τ_{Ge} vs. δ^{74}Ge; (c) Ge/Si ratio vs. δ^{74}Ge for different samples from the Wenchang basalt weathering profile. The filled legends represent that the samples were excluded from the statistics. (d) Fluvial Ge/Si ratio vs. δ^{74}Ge for the rivers with different watershed rock types (after Baronas et al., 2017a).

those of basalt (δ^{74}Ge = 0.54‰), indicate that light Ge isotopes are preferentially retained and enriched in the solid weathering products. The Ge isotope fractionation during basalt weathering can be further simulated using an estimated ε of -1.38 ± 0.28‰ (2σ) (corresponding to $\alpha_{Solid-Dissolved} = 0.99862$, see discussion below). The simulated results indicate that (1) there are distinct $\delta^{74}Ge_S$ and τ_{Ge} correlations in the solid weathering products, and (2) $\delta^{74}Ge_S$ is always lower than $\delta^{74}Ge_B$; during the Ge leaching ($\tau_{Ge} < 0$) process of basalt weathering or progressive weathering of solid weathering products (Fig. 6a and b).

The chemical mobility (dissolved concentration in rivers/continental abundance) of Si is similar to that of Na, while that of Ge is 10–100 times less than that of sodium; Ge has been regarded as an immobile element during weathering and riverine transport processes (Gaillardet et al., 2014). Such low chemical mobility implies that: (1) the Ge released from the leaching of upper sub-horizons (soil and/or saprolite) during progressive weathering or pedogenic processes would be mainly retained in the lower part of the soil and/or saprolite, and (2) the vertical migration distance of dissolved Ge would be limited. These hypotheses are supported by the alternative depletion-enrichment of Ge and δ^{74}Ge in the soils and saprolites across the weathering profile, which indicate distinct internal redistribution and local enrichment of Ge ($\tau_{Ge} > 0$). According to the prediction results of the batch equilibrium or Rayleigh-type model, it is impossible for saprolite samples from 4 to 6 m deep or near the saprolite-bedrock interface to have heavier (or similar) $\delta^{74}Ge_S$ (up to 0.65 ± 0.10‰), or lighter $\delta^{74}Ge_S$ (-0.03 ± 0.10‰) and τ_{Ge} (−0.03) at 14.04 m deep (relative to average δ^{74}Ge of basalts) without any pedogenic redistribution or re-equilibration.

For the soil and saprolite samples with positive τ_{Ge}, their $\delta^{74}Ge_S$ can be approximated by the mixing of the average value ($\delta^{74}Ge_{average}$) of selected soil or saprolite samples (e.g., the upper Ge depleted (lighter δ^{74}Ge) and lower Ge enriched (heavier δ^{74}Ge) samples within certain depth) and heavy pore fluids ($\delta^{74}Ge_D$) leached from the upper

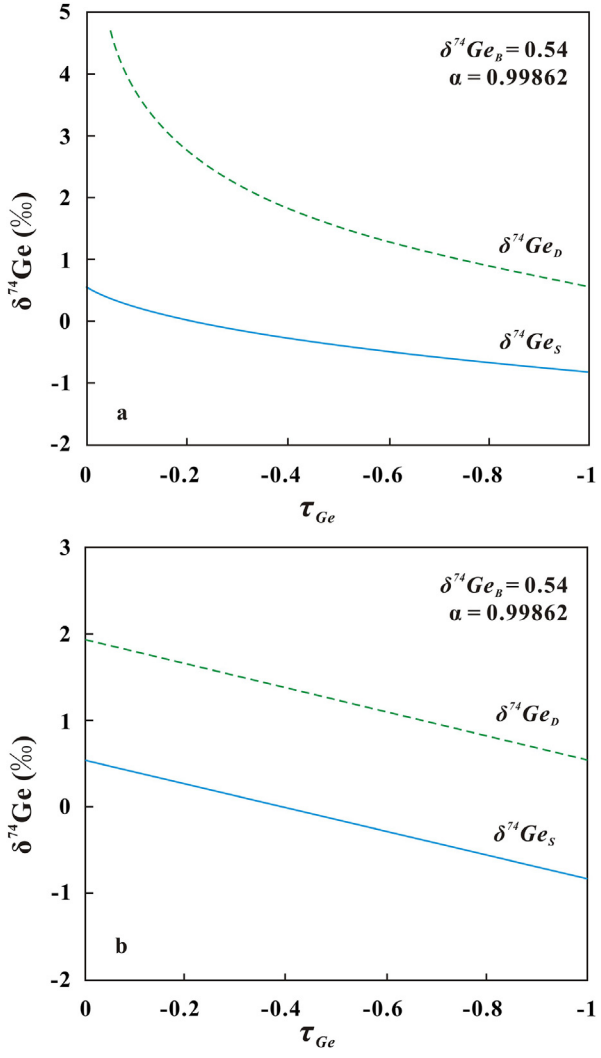

Fig. 6. Evolution of Ge isotope compositions of dissolved phase ($\delta^{74}Ge_D$) and solid weathering product ($\delta^{74}Ge_S$), as a function of the proportion of Ge removal during basalts weathering. (a) Rayleigh-type fractionation model; (b) Steady-state fractionation model. An initial Ge isotope composition of basalts ($\delta^{74}Ge_B$) of 0.54‰ and an equilibrium fractionation factors (1000 * Ln(α) = −1.38‰ (2σ)) were selected.

depleted samples with a proportion of τ_{Ge} (Eqs. (9) and (10)). In this model, τ_{Ge} should be calculated relative to the average composition of selected soil or saprolite samples. A similar way has been used to estimate the variations of $\delta^{30}Si$ of paleosols influenced by fluid percolation (Delvigne et al., 2016).

$$\delta^{74}Ge_D = \delta^{74}Ge_{average} - \varepsilon * (1 - \tau_{Ge}) \quad (9)$$

$$\delta^{74}Ge_S = \delta^{74}Ge_{average} + \tau_{Ge} * \delta^{74}Ge_D \quad (10)$$

We used this model to estimate the $\delta^{74}Ge_S$ of the most Ge-enriched saprolite samples near the soil-saprolite or saprolite-bedrock interface. For example, using the average composition ($\delta^{74}Ge_{average} = 0.24‰$) of 15 samples (WC-1 to WC-15), the same ε (−1.38 ±0.28‰ (2σ)), and the recalculated τ_{Ge} values (0.25–0.40), the estimated $\delta^{74}Ge_S$ for these Ge-enriched samples (WC-13, WC-14, and WC-15) are of 0.56–0.67‰. Similarly, based on the $\delta^{74}Ge_{average}$ (0.35‰) of nine samples (WC-44 to WC-52) and the recalculated τ_{Ge} values (0.22–0.39), the estimated $\delta^{74}Ge_S$ for the saprolite samples WC-50, WC-51, and WC-52 are 0.66–0.81‰. These estimated $\delta^{74}Ge_S$ values are slightly higher than those of measured values (0.40–0.63‰) within the uncertainty of ±0.28‰ (2σ) for ε.

5.4. Possible influence on fluvial Ge isotope fractionation and global Ge-Si cycle

5.4.1. Estimation of $\delta^{74}Ge_D$, Ge/Si_D signature and fractionation factor

The $\delta^{74}Ge_D$ and Ge/Si_D of the soil solutions from the studied profile were estimated with the mass balance equations (Eqs. (2) and (3), Supplement C), using basalt as the reactant and soil and saprolite as the product. The calculated solution composition is an integrated solution that reflects the changes from bedrock to saprolite (or from saprolite to soil), because both the solid products and pore waters captures only a snapshot of the fluid-solid interactions, and the signatures perhaps may have been overprinted by the re-equilibration with local solids during progressive weathering or pedogenic processes (Lugolobi et al., 2010; this study). These mass balance equations are only suitable for the cases where Ge is lost (for negative τ_{Ge} samples), and they yield physically impossible negative Ge/Si_D values for positive τ_{Ge} samples (Table 1). Theoretically, positive τ_{Ge} values imply that the dissolved Ge would be absorbed by the solid weathering products, and that the Ge/Si ratios of dissolved phase would decrease to near zero with increasing positive τ_{Ge} values. This also indicates that the solid weathering products have been influenced by the addition of isotopically heavy Ge, e.g., from reprecipitation or readsorption from heavy pore fluids. Moreover, prediction results of the Rayleigh fractionation model show that (1) with increasing negative τ_{Ge} value, the observed Ge isotopic difference between the solid products and dissolved phase or fluid ($\delta^{74}Ge_S$–$\delta^{74}Ge_D$) would gradually converge to close to the fractionation factor ($\Delta^{74}Ge_{solid\text{-}dissolved} = 1000 * Ln(\alpha)$ or ε); (2) lower absolute τ_{Ge} (or higher $\delta^{74}Ge_D$), likely results in very high Δ uncertainty for the preferential enrichment of heavy Ge isotope in the dissolved phase (Fig. 6a). The fractionation factor can also be estimated by the Ge isotopic difference between the solid product and basalt, which accounts for the fraction of Ge lost ($\Delta^{74}Ge_{solid\text{-}dissolved} = (\delta^{74}Ge_S - \delta^{74}Ge_B)/(-\tau_{Ge})$), based on Eq. (8). Both methods yielded identical results (Table 1, Fig. 7). It is noteworthy that with more negative τ_{Ge} (<−0.19), Δ values converge to −1.38 ± 0.28‰ (2σ) (n = 7), which likely represent the actual fractionation factor during weathering. The Wenchang basalt weathering profile has been overprinted by progressive weathering of the solid weathering products, and it is impossible to connect the present τ_{Ge} value with the instantaneous fraction of Ge remained in the solutions during the different basalt weathering stage (initial or progressive weathering). Therefore, the estimated fractionation factor represents only an

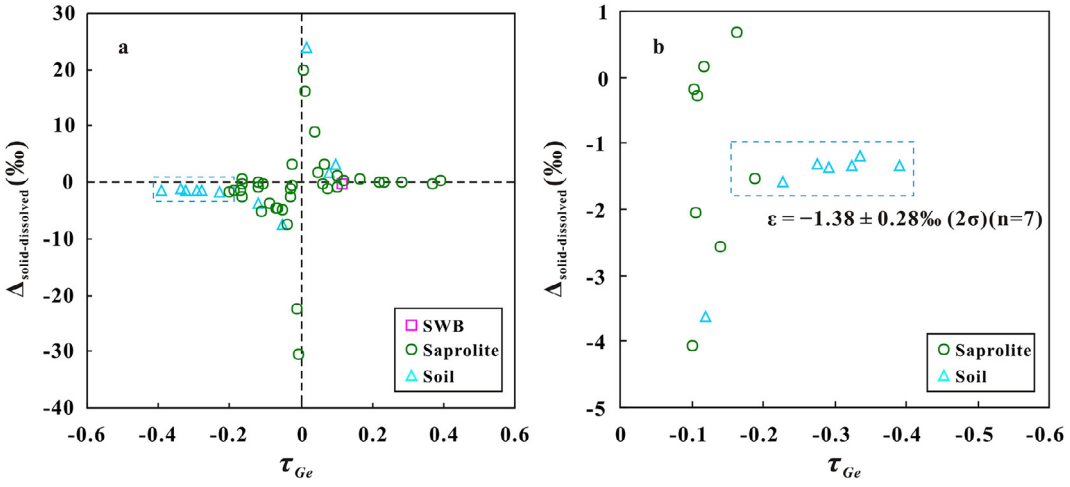

Fig. 7. The estimated fractionation factor ($\Delta_{solid\text{-}dissolved} = 1000 * Ln(\alpha)$) as a function of τ_{Ge} value during basalt weathering. (a) most soil and saprolite samples with positive or negative τ_{Ge} value, while the samples with near-zero absolute τ_{Ge} (which yielded highly positive (>30) or negative (<−40) $\Delta_{solid\text{-}dissolved}$) were excluded; (b) soil and saprolite samples with highly negative τ_{Ge} value ($\tau_{Ge} < -0.1$).

integrated or long-term trend of the whole weathering history.

5.4.2. Comparison with riverine $\delta^{74}Ge$ and Ge/Si signatures

Prediction results of the Rayleigh fractionation model suggest both $\delta^{74}Ge_S$ and $\delta^{74}Ge_D$ would decrease with increasing negative τ_{Ge} in the solid weathering products, while their Ge/Si_D would correlated positively with τ_{Ge} and negatively with τ_{Si} of solid weathering products ($Ge/Si_D = Ge/Si_B * \tau_{Ge}/\tau_{Si}$, Supplement C). Shallow soils generally experience more extensive Ge leaching than deep saprolites. Therefore, depending on the different mobility of Ge and Si, the shallow pore water released by progressive weathering of soils and the deep pore water released by progressive weathering of deep saprolites (or those released during the 'initial' weathering of basalts) should have different Ge/Si_D and $\delta^{74}Ge_D$. Theoretically, there should be a negative Ge/Si_D vs. $\delta^{74}Ge_D$ correlation for pore water. Moreover, the preferential adsorption of light Ge isotopes by deep solid weathering products during progressive weathering of shallow solid weathering products would lead to heavier $\delta^{74}Ge_D$ value in the infiltrated pore water. Although there are large errors in the simulation, the stepwise weathering model and mass balance calculation results indicate that the dissolved phase (or released pore water) in the basalt-saprolite weathering transformation would yield lower Ge/Si_D (0.12 ± 0.02 (1σ) μmol/mol) but higher $\delta^{74}Ge_D$ (7.40 ± 3.63 ‰ (1σ)), relative to those ($Ge/Si_D = 5.74 \pm 1.68$ (1σ) μmol/mol, $\delta^{74}Ge_D = 1.43 \pm 0.96$‰ (1σ)) of the pore water released in the saprolite-soil weathering transformation (Table 2).

These hypotheses and calculated results match the published data of river water and pore water. For example, the dissolved $\delta^{74}Ge$ compositions of analyzed river water from California, Hawaii, and Peru range from 2.0 to 5.6‰, which correlate well with the dissolved Ge concentrations (68–809 pM) and Ge/Si ratios (0.24–1.88 μmol/mol) (Baronas et al., 2017a). For the actual pore water from silicate weathering environment, Ziegler et al. (2005) and Lugolobi et al. (2010) found that shallow saprolite and soil water contain higher Ge/Si (up to 4.0 μmol/mol) and than those (0.27–0.47 μmol/mol) of deep saprolite and baseflow streams from Puerto Rico. Furthermore, the predicted negative Ge/Si_D vs. $\delta^{74}Ge_D$ correlation for pore water is supported by the negative Ge/Si vs. $\delta^{74}Ge$ correlation in river water (Fig. 5d; Baronas et al., 2017a). These theoretical considerations and calculations provide some important guidelines for the interpretations of riverine Ge/Si and $\delta^{74}Ge$ signatures (if Ge isotope fractionations during transportation were neglected), e.g., the end-member with high $\delta^{74}Ge$ but low Ge/Si in the river water may be derived from two different sources: (1) the initial weathering of parent rocks; and (2) the progressive weathering of deep solid weathering products, while the end-member with low $\delta^{74}Ge$ but high Ge/Si may be mainly derived via progressive weathering of shallow soil or saprolite. Moreover, all sources of Ge to the ocean in the recent global Ge isotope budget were balanced by the burial of diatom, sponge and non-opal authigenic minerals in marine sediments (i.e., Baronas et al., 2017a). The rivers input about 20% of total Ge source-fluxes into the ocean (Baronas et al., 2017a), however, the possible influence of solid weathering products on the riverine Ge/Si and $\delta^{74}Ge$ signatures was not considered. Our results indicate that solid weathering products are a sink for light Ge isotopes, possible to balance the budget (such as river and seawater) with heavy Ge isotope compositions.

6. CONCLUSIONS

Germanium concentrations and Ge/Si ratios of the soil and saprolite samples from Wenchang are distinctly higher than those of the fresh basalts. Compared to the relative homogeneous Ge isotope composition of the fresh basalt, the $\delta^{74}Ge$ values of most soil and saprolite samples are in general lower than those of the fresh basalt samples, and

exhibit complex vertical fluctuation. There are no distinct correlations between the concentrations of Ge (or Ge/Si or δ^{74}Ge) and SiO_2, Al_2O_3, Fe_2O_3 and MnO for most soil and saprolite samples. The distinct positive δ^{74}Ge vs. Ge content correlations (or τ_{Ge} and Ge/Si) for most soil and saprolite samples indicate that the enrichment (or depletion) of Ge content, Ge isotopes and Ge/Si fractionation are controlled by a common sorption process of the solid weathering products. The positive Ge/Si vs. δ^{74}Ge correlation of most soil and saprolite samples from the Wenchang basalt weathering profile, and the negative one of published river water data, demonstrate that soil and river data are complementary. Moreover, the estimated negative $\Delta^{74}Ge_{solid\text{-}dissolved}$ (1000 * Ln(α)) value indicates that light Ge isotopes are preferentially retained and enriched in the solid weathering products, which can possibly balance the isotopic budget with heavy Ge isotope compositions in rivers and oceans.

ACKNOWLEDGMENTS

This project was financially supported by National Natural Science Foundation of China (grant no. 41073041, 41673052). The authors appreciate the constructive comments and suggestions of J. Jotautas Baronas (University of Cambridge), Anthony Dosseto (Associate Editor) and an anonymous reviewer, which significantly improved the quality of data interpretation of the manuscript. Language editing service by Cenozoic Editing & Consultancy (Australia) is acknowledged.

APPENDIX A. SUPPLEMENTARY MATERIAL

Supplementary data to this article can be found online at https://doi.org/10.1016/j.gca.2019.03.022.

REFERENCES

Anders A. M., Sletten R. S., Derry L. A. and Hallet B. (2003) Germanium/silicon ratios in the Copper River Basin, Alaska: WEATHERING and partitioning in periglacial versus glacial environments. *J. Geophys. Res.* **108**(F1), 1–9.

Arnórsson S. (1984) Germanium in Icelandic geothermal systems. *Geochim. Cosmochim. Acta* **48**, 2489–2502.

Babechuk M. G., Widdowson M. and Kamber B. S. (2014) Quantifying chemical weathering intensity and trace element release from two contrasting basalt profiles, Deccan Traps, India. *Chem. Geol.* **363**, 56–75.

Baronas J. J., Hammond D. E., Berelson W. M., McManus J. and Severmann S. (2016) Germanium –silicon fractionation in a river-influenced continental margin: the Northern Gulf of Mexico. *Geochim. Cosmochim. Acta* **178**, 124–142.

Baronas J. J., Hammond D. E., McManus J., Wheat C. G. and Siebert C. (2017a) A global Ge isotope budget. *Geochim. Cosmochim. Acta* **203**, 265–283.

Baronas J. J., Torres M. A., Clark K. E. and West A. J. (2017b) Mixing as a driver of temporal variations in river hydrochemistry: 2. Major and trace element concentration dynamics in the Andes-Amazon transition. *Water Resour. Res.* **53**, 3120–3145.

Berner R. A., Lasaga A. C. and Garrels R. M. (1983) The carbonate–silicate geochemical cycle and its effect on atmospheric carbon-dioxide over the past 100 million years. *Am. J. Sci.* **283**, 641–683.

Bernstein L. R. (1985) Germanium geochemistry and mineralogy. *Geochim. Cosmochim. Acta* **49**, 2409–2422.

Bernstein L. R. and Waychunas G. A. (1987) Germanium crystal chemistry in hematite and goethite from the Apex Mine, Utah, and some new data on germanium in aqueous solution and in stottite. *Geochim. Cosmochim. Acta* **51**, 623–630.

Brady P. V. and Carroll S. A. (1994) Direct effects of CO2 and temperature on silicate weathering: Possible implications for climate control. *Geochim. Cosmochim. Acta* **58**, 1853–1856.

DeArgollo R. and Schilling J. G. (1978) Ge-Si and Ga-Al fractionation in Hawaiian volcanic rocks. *Geochim. Cosmochim. Acta* **42**, 623–630.

Delvigne C., Opfergelt S., Cardinal D., Hofmann A. and André L. (2016) Desilication in Archean weathering processes traced by silicon isotopes and Ge/Si ratios. *Chem. Geol.* **420**, 139–147.

Derry L. A., Kurtz A. C., Ziegler K. and Chadwick O. A. (2005) Biological control of terrestrial silica cycling and export fluxes to watersheds. *Nature* **433**, 728–731.

Derry L. A., Pett-Ridge J. C., Kurtz A. C. and Troester J. W. (2006) Ge/Si and $^{87}Sr/^{86}Sr$ tracers of weathering reactions and hydrologic pathways in a tropical granitoid system. *J. Geochem. Explorat.* **88**, 271–274.

Escoube R., Rouxel O. J., Luais B., Ponzevera E. and Donard O. F. X. (2012) Intercomparison study of Germanium isotope composition of natural and synthetic geochemical reference materials. *Geostand. Geoanal. Res.* **36**, 149–159.

Escoube R., Rouxel O. J., Edwards K., Glazer B. and Donard O. F. X. (2015) Coupled Ge/Si and Ge isotope ratios as geochemical tracers of seafloor hydrothermal systems: case studies at Loihi Seamount and East Pacific Rise 9°50′N. *Geochim. Cosmochim. Acta* **167**, 93–112.

Froelich P. N., Blanc V., Mortlock R. A., Chillrud S. N., Dunstan W., Udomkit A. and Peng T.-H. (1992) River fluxes of dissolved silica to the ocean were higher during the glacials: Ge/Si in diatoms, rivers, and oceans. *Paleoceanography* **7**, 739–767.

Froelich P. N., Hambrick G. A., Andreae M. O., Mortlock R. A. and Edmond J. M. (1985) The geochemistry of inorganic germanium in natural waters. *J. Geophys. Res.* **90**(C1), 1133–1141.

Gaillardet J., Dupré B., Louvat P. and Allègrea C. J. (1999) Global silicate weathering and CO2 consumption rates deduced from the chemistry of large rivers. *Chem. Geol.* **159**, 3–30.

Gaillardet J., Viers J. and Dupre B. (2014) Trace elements in river waters. *Treatise Geochem.* **5**(Suppl 1), 195–235.

Georg R. B., Reynolds B. C., West A. J., Burton K. W. and Halliday A. N. (2007) Silicon isotope variations accompanying basalt weathering in Iceland. *Earth Planet. Sci. Lett.* **261**, 476–490.

Guillermic M., Lalonde S. V., Hendry K. R. and Rouxel O. J. (2017) The isotope composition of inorganic germanium in seawater and deep sea sponges. *Geochim. Cosmochim. Acta* **212**, 99–118.

Hughes H. J., Sondag F., Santos R. V., André L. and Cardinal D. (2013) The riverine silicon isotope composition of the Amazon Basin. *Geochim. Cosmochim. Acta* **121**, 637–651.

Jiang K., Qi H. W. and Hu R. Z. (2018) Element mobilization and redistribution under extreme tropical weathering of basalts from the Hainan Island, South China. *J. Asian Earth Sci.* **158**, 80–102.

King S., Froelich P. and Jahnke R. (2000) Early diagenesis of germanium in sediments of the Antarctic South Atlantic: in search of the missing Ge sink. *Geochim. Cosmochim. Acta* **64**, 1375–1390.

Kurtz A. C., Derry L. A. and Chadwick O. A. (2002) Germanium-silicon fractionation in the weathering environment. *Geochim. Cosmochim. Acta* **66**, 1525–1537.

Kurtz A. C., Derry L. A., Chadwick O. A. and Alfano M. J. (2000) Refractory element mobility in volcanic soils. *Geology* **28**, 683–686.

Li X. F. and Liu Y. (2010) First-principles study of Ge isotope fractionation during adsorption onto Fe(III)-oxyhydroxides surfaces. *Chem. Geol.* **278**, 15–22.

Li X. F., Zhao H., Tang M. and Liu Y. (2009) Theoretical prediction for several important equilibrium Ge isotope fractionation factors and geological implications. *Earth Planet. Sci. Lett.* **287**, 1–11.

Liu J. Q., Ren Z. Y., Nichols A. R. L., Song M. S., Qian S. P., Zhang Y. and Zhao P. P. (2015) Petrogenesis of Late Cenozoic basalts from North Hainan Island: constraints from melt inclusions and their host olivines. *Geochim. Comochim. Acta* **152**, 89–121.

Luais B. (2012) Germanium chemistry and MC-ICPMS isotopic measurements of Fe–Ni, Zn alloys and silicate matrices: Insights into deep Earth processes. *Chem. Geol.* **334**, 295–311.

Lugolobi F., Kurtz A. C. and Derry L. A. (2010) Germanium–silicon fractionation in a tropical, granitic weathering environment. *Geochim. Cosmochim. Acta* **74**, 1294–1308.

Ma J. L., Wei G. J., Xu Y. G., Long W. G. and Sun W. D. (2007) Mobilization and re-distribution of major and trace elements during extreme weathering of basalt in Hainan Island, South China. *Geochim. Comochim. Acta* **71**, 3223–3237.

Ma J. L., Wei G. J., Xu Y. G. and Long W. G. (2010) Variations of Sr–Nd–Hf isotopic systematics in basalt during intensive weathering. *Chem. Geol.* **269**, 376–385.

McLennan S. M. (1993) Weathering and global denudation. *J. Geol.* **101**, 295–303.

McManus J., Hammond D. E., Cummins K., Klinkhammer G. P. and Berelson W. M. (2003) Diagenetic Ge/Si fractionation in continental margin environments: further evidence for a nonopal Ge sink. *Geochim. Cosmochim. Acta* **67**, 4545–4557.

Meek K., Derry L., Sparks J. and Cathles L. (2016) $^{87}Sr/^{86}Sr$, Ca/Sr, and Ge/Si ratios as tracers of solute sources and biogeochemical cycling at a temperate forested shale catchment, central Pennsylvania, USA. *Chem. Geol.* **445**, 84–102.

Meng Y. M., Qi H. W. and Hu R. Z. (2015) Determination of germanium isotopic compositions of sulfides by hydride generation MC-ICP-MS and its application to the Pb–Zn deposits in SW China. *Ore Geol. Rev.* **65**, 1095–1109.

Mortlock R. A. and Froelich P. N. (1986) Hydrothermal germanium over the Southern East Pacific Rise. *Science* **231**, 43–45.

Mortlock R. A. and Froelich P. N. (1987) Continental weathering of germanium: Ge/Si in the global discharge. *Geochim. Cosmochim. Acta* **51**, 2075–2082.

Mortlock R. A., Froelich P. N., Feely R. A., Massoth G. J., Butterfield D. A. and Lupton J. E. (1993) Silica and germanium in Pacific Ocean hydrothermal vents and plumes. *Earth Planet. Sci. Lett.* **119**, 365–378.

Murnane R. J. and Stallard R. F. (1990) Germanium and silicon in rivers of the Orinoco drainage basin. *Nature* **344**, 749–752.

Nesbitt H. W. and Young G. M. (1982) Early Proterozoic climates and plate motions inferred from major element chemistry of lutites. *Nature* **299**, 715–717.

Nesbitt H. W. and Wilson R. E. (1992) Recent chemical weathering of basalts. *Am. J. Sci.* **292**, 740–777.

Pokrovsky O. S. and Schott J. (2002) Iron colloids/organic matter associated transport of major and trace elements in small boreal rivers and their estuaries (NW Russia). *Chem. Geol.* **190**, 141–179.

Pokrovsky O. S., Galy A., Schott J., Pokrovski G. S. and Mantoura S. (2014) Germanium isotope fractionation during Ge adsorption on goethite and its coprecipitation with Fe oxy (hydr)oxides. *Geochim. Cosmochim. Acta* **131**, 138–149.

Qi H. W., Rouxel O., Hu R. Z., Bi X. W. and Wen H. J. (2011) Germanium isotopic systematics in Ge-rich coal from the Lincang Ge deposit, Yunnan, Southwestern China. *Chem. Geol.* **286**, 252–265.

Rouxel O. J. and Luais B. (2017) Germanium Isotope Geochemistry. *Rev. Mineral. Geochem.* **82**, 601–656.

Rouxel O., Galy A. and Elderfield H. (2006) Germanium isotopic variations in igneous rocks and marine sediments. *Geochim. Cosmochim. Acta* **70**, 3387–3400.

Scribner A. M., Kurtz A. C. and Chadwick O. A. (2006) Germanium sequestration by soil: targeting the roles of secondary clays and Fe-oxyhydroxides. *Earth Planet. Sci. Lett.* **243**, 760–770.

Taylor S. R. and McLennan S. M. (1985) *The Continental Crust: its Composition and Evolution*. Blackwell Scientific Publications, Oxford, pp. 9–67.

Tipper E. T., Louvat P., Capmas F., Galy A. and Gaillardet J. (2008) Accuracy of stable Mg and Ca isotope data obtained by MC-ICP-MS using the standard addition method. *Chem. Geol.* **257**, 65–75.

Walker J. C. G., Hays P. B. and Kasting J. F. (1981) A negative feedback mechanism for the long-term stabilization of Earth's surface temperature. *J. Geophys. Res. – Oceans Atmos* **86**, 9776–9782.

Wang Z. B., Ma J. L., Li J., Wei G. J., Zeng T., Li L., Zhang L., Deng W. F., Xie L. H. and Liu Z. F. (2018) Fe (hydro) oxide controls Mo isotope fractionation during the weathering of granite. *Geochim. Cosmochim. Acta* **226**, 1–17.

Wheat C. G. and McManus J. (2005) The potential role of ridge-flank hydrothermal systems on oceanic germanium and silicon balances. *Geochim. Cosmochim. Acta* **69**, 2021–2029.

Wiche O. and Heilmeier H. (2016) Germanium (Ge) and rare earth element (REE) accumulation in selected energy crops cultivated on two different soils. *Miner. Eng.* **92**, 208–215.

Wille M., Babechuk M. G., Kleinhanns I. C., Stegmaier J., Suhr N., Widdowson M., Kamber B. S. and Schoenber R. (2018) Silicon and chromium stable isotopic systematics during basalt weathering and lateritisation: a comparison of variably weathered basalt profiles in the Deccan Traps, India. *Geoderma* **314**, 190–204.

Ziegler K., Chadwick O. A., Brzezinski M. A. and Kelly E. F. (2005) Natural variations of $\delta^{30}Si$ ratios during progressive basalt weathering, Hawaiian Islands. *Geochim. Cosmochim. Acta* **69**, 4597–4610.

Associate editor: Anthony Dosseto